Experimental study on water-wave trapped modes

P. J. COBELLI[1]†, V. PAGNEUX[2],
A. MAUREL[3] AND P. PETITJEANS[1]

[1]Laboratoire de Physique et Mécanique des Milieux Hétérogènes, UMR CNRS 7636, Ecole Supérieure de Physique et de Chimie Industrielles, 10 rue Vauquelin, 75231 Paris CEDEX 5, France

[2]Laboratoire d'Acoustique de l'Université du Maine, UMR CNRS 6613, Avenue Olivier Messiaen, 72085 Le Mans CEDEX 9, France

[3]Laboratoire Ondes et Acoustique, Institut Langevin UMR CNRS 7587, Ecole Supérieure de Physique et de Chimie Industrielles, 10 rue Vauquelin, 75231 Paris CEDEX 5, France

We present an experimental study on the trapped modes occurring around a vertical surface-piercing circular cylinder of radius a placed symmetrically between the parallel walls of a long but finite water waveguide of width $2d$. A wavemaker placed near the entrance of the waveguide is used to force an asymmetric perturbation into the guide, and the free-surface deformation field is measured using a global single-shot optical profilometric technique. In this configuration, several values of the aspect ratio a/d were explored for a range of driving frequencies below the waveguide's cutoff. Decomposition of the obtained fields in harmonics of the driving frequency allowed for the isolation of the linear contribution, which was subsequently separated according to the symmetries of the problem. For each of the aspect ratios considered, the spatial structure of the trapped mode was obtained and compared to the theoretical predictions given by a multipole expansion method. The waveguide–obstacle system was further characterized in terms of reflection and transmission coefficients, which led to the construction of resonance curves showing the presence of one or two trapped modes (depending on the value of a/d), a result that is consistent with the theoretical predictions available in the literature. The frequency dependency of the trapped modes with the geometrical parameter a/d was determined from these curves and successfully compared to the theoretical predictions available within the frame of linear wave theory.

Key words: surface gravity waves, wave–structure interactions, wave scattering

1. Introduction

In the framework of the classical theory of linearized water waves in unbounded domains, trapped modes consist of non-propagative localized oscillation modes of finite energy occurring at some well-defined frequency and which, in the absence of dissipation, persist in time even in the absence of external forcing.

The first theoretical example of such trapping mode in the theory of water waves, due to Stokes (1846), consists of waves which travel in the long-shore direction over

† Email address for correspondence: cobelli@pmmh.espci.fr

a uniformly sloping beach and decay to zero in the seaward direction. Such a trapped mode has often been referred to as an edge wave, as, in this case, the energy remains trapped near the shore. (Note that, in this case, finite energy is to be understood in terms of energy per unit length along the shore.) These localized modes were later generalized by Ursell (1952) to an infinite set of discrete modes, of which Stokes' edge waves represent the fundamental mode. For a recent review on edge waves, the reader is referred to Johnson (2007) and references therein. Field observations of edge waves have been reported by Huntley & Bowen (1973). For a description of edge waves in an oceanographic context, the reader is referred to the work of LeBlond & Mysak (1978).

Ursell (1951) showed that such a trapped mode could also exist in the vicinity of a long submerged horizontal circular cylinder, in the form of waves travelling along the cylinder and decaying in a direction normal to the cylinder axis. His proof, originally restricted to sufficiently small cylinders (i.e. of radius smaller than the wavelength), was later extended by Jones (1953). Indeed, employing a general treatment based on the theory of elliptic partial differential equations in unbounded domains, this latter author proved that trapped modes exist for a submerged horizontal cylinder of symmetric but otherwise arbitrary cross-section, both in finite and infinite depth. Finally, a proof based on Kelvin's minimum-energy theorem was provided by Ursell (1987) for the existence of trapped modes in the case of a totally submerged body without any restriction on its shape and size. Moreover, in a numerical study, McIver & Evans (1985) showed that there is always at least one trapped mode above a cylinder of arbitrary size and that further modes are possible as the top of the cylinder approaches the free surface.

More importantly, Jones' work proved the existence of trapping modes for problems governed by the Helmholtz equation in semi-infinite domains, indicating that such bound states could occur (under certain conditions) in other contexts such as acoustics. Evans & Linton (1991) described a constructive method for determining trapped-mode frequencies in two specific problems in which the two-dimensional Helmholtz equation is satisfied, and which were not covered directly by Jones' theory. One of these problems involves the free-surface fluid motion in a long waveguide containing a vertical cylinder of uniform cross-section placed symmetrically between its walls and extending throughout the water depth. In this case, separation of the depth dependance leaves out the Helmholtz equation and the dispersion relation linking the wavenumber and the wave frequency, required to satisfy the linearized free-surface condition for water waves. Neumann boundary conditions on the walls set a threshold for the propagation of perturbations which are antisymmetric with respect to the waveguide centreplane. Below this cutoff frequency, antisymmetric waves cannot propagate, though they may still exist within the guide in the form of evanescent waves. Although trapped-mode solutions, localized within the waveguide and having bounded total energy, are not possible below this cutoff, Evans & Linton (1991) showed that the presence of a symmetrically placed rectangular block satisfying a no-flow condition on its sides and having two sides parallel to the waveguide walls enabled the construction of such solutions, and computed their frequencies. These modes are characterized by having finite total energy, being localized in the vicinity of the obstacle and decaying rapidly to zero with distance down the waveguide. Moreover, the number of such modes increases with the length of the block; conversely, only a single mode exists for a block shorter than the channel width. This study provided numerical evidence as well as a criterion as to when to expect such modes to occur for this class of problems and how to compute them.

McIver (1991) derived the trapped-mode frequency for antisymmetric trapped modes in the vicinity of a vertical cylinder of arbitrary but small cross-section in a water channel of infinite extent. Similar results were obtained by Evans & McIver (1991) for the trapped-mode frequency close to the cutoff, for the particular case of symmetric thin bodies.

Callan, Linton & Evans (1991), employing a method due to Ursell (1951), proved the existence of a trapped mode for a cylinder of sufficiently small radius placed symmetrically within the guide. Furthermore, an explicit relation between the cylinder radius, the waveguide width and the trapped-mode frequency was found in this particular case. However, numerical computations revealed that a single trapped surface wave mode exists irrespective of the cylinder size. Moreover, it was also shown that, in the general case, the frequency of the trapped-mode oscillation lies below the fundamental cutoff frequency for the channel and depends only upon the ratio of cylinder radius to waveguide width. This trapped mode, having a frequency close but below the fundamental cutoff frequency of the channel, is characterized by being antisymmetric about the centreplane of the guide and symmetric about a line perpendicular to the waveguide walls passing through the cylinder axis (hereafter termed Neumann-symmetric, or NS-trapped modes). However, no trapped modes antisymmetric about both lines (Neumann-antisymmetric, or NA-trapped modes) were found in this study.

In relation to this problem, Linton & Evans (1992) constructed a homogeneous integral equation for the trapped modes in the case of a cylinder of fairly general cross-section and showed that the trapped-mode frequencies agreed numerically with the previous results for the circular cross-sections. Evans, Levitin & Vassiliev (1994) showed that there is at least one trapped mode antisymmetric about the centreplane of the waveguide, localized near an obstacle of symmetric but otherwise fairly general shape about the centreline of the waveguide and decaying with distance down the guide away from the obstacle.

Evans & Porter (1999) described a method for constructing trapped modes antisymmetric about the line through the centre of the cylinder and perpendicular to the channel walls (i.e. NA-trapped modes). Their numerical computations of such modes established their existence for values of the control parameter in excess of a numerically determined threshold, corresponding to cylinders of radius 0.81 times larger than the waveguide's width.

In the last 15 years, the study of trapped modes has developed and diversified. McIver (1996) was the first to construct a finite structure supporting a so-called sloshing trapped mode. These sloshing trapping structures have two surface-piercing elements separated by a portion of the free surface, the fluid motion being essentially confined to the region inside the structure. Modifications of the construction method employed by McIver (1996) have now been used to build a variety of sloshing trapping structures in two and three dimensions, both submerged (see McIver 2000; Evans & Porter 2002; McIver & Porter 2002) and surface-piercing (see Kuznetsov & McIver 1997; McIver & McIver 1997; McIver & Newman 2003). Coupled oscillations between a freely floating structure and the surrounding fluid, termed 'motion trapped modes', were recently obtained by McIver & McIver (2006). The distinguishing characteristic of these recent studies is that there is no cutoff frequency for propagation and hence the trapped-mode frequencies are embedded in the continuous spectrum. For more information on recent developments in the study of trapped modes, the reader is referred to the comprehensive review given by Linton & McIver (2007). Also note that trapped modes occur in different forms in various domains of physics, such as

quantum mechanics, elasticity, acoustics, etc. (Londergan, Carini & Murdock 1999; Pagneux 2006; Zernov, Pichugin & Kaplunov 2006; Postnova & Craster 2008).

It is worth noting that, as pointed out by Harter, Abrahams & Simon (2007), none of the studies cited above accounts for the effect of surface tension. In particular, no condition is included to describe the motion of the fluid at the contact line, based on the argument that such a condition would have a significant effect for small values of surface tension. As a consequence, the question arises as to whether its effects might play a relevant role in the observation of trapped modes, and to whether it is physically realistic to exclude surface tension from the linear water-wave problem. Moreover, as, at present, the contact-line problem is not well understood and there is no general agreement within the academic community as to what condition should be applied, experimental studies are indeed particularly valuable.

In the framework of the present experimental study, we will focus on the measurement and analysis of trapped modes occurring around a vertical surface-piercing circular cylinder placed symmetrically between the parallel walls of a long but finite water waveguide. It is worth noting here that the finite length of the waveguide, even on the basis of inviscid linear theory, leads to a complex resonance (i.e. a near-trapped mode), since the wave can always leak out of the waveguide. The presence of dissipation also participates to this leakage.

The trapped modes associated to this configuration are also of interest to acoustics, as they also describe acoustic resonances associated with a two-dimensional acoustic waveguide containing a sound–hard (cylindrical) obstacle, by virtue of the separation of the depth factor in the water-wave problem.

Another aspect of interest regarding this particular configuration arises from the consideration of the Neumann (no-flow) boundary conditions at the waveguide walls. Indeed, neglecting the effects of the boundary layer, the walls can equally well be thought of as representing lines of symmetry. Hence, these trapped modes also exist in the presence of an infinite linear array of regularly spaced obstacles, generating very large forces on the elements of the array (see Evans & Porter 1997*a*,*b*; Maniar & Newman 1997). Moreover, Evans & Porter (1999) showed that 'near-trapping' could occur between adjacent elements within a large but otherwise *finite* array of cylinders. In this case, it was found that the associated near-trapping frequencies are related to the Rayleigh–Bloch trapped-wave frequencies for the infinite array. (See Linton & McIver 2002 for a discussion on the existence of Rayleigh–Block waves.) In practice, the occurrence of near-trapped modes is of particular relevance to offshore structures based on a large number of piles (such as oil rigs, very large floating structures and breakwaters) as it implies the presence of very large loads on individual elements of the array. Recent progress in the understanding of wave interaction with arrays of offshore structures, resonant effects and their consequences for finite arrays has been discussed by McIver (2002).

In marked contrast to the large number of theoretical studies concerned with existence proofs and numerical algorithms for the computation of trapped modes for different geometries, little attention appears to have been paid to their experimental observation, characterization and analysis.

Indeed, the only experimental results available in the literature for the problem under study are due to Retzler (2001). In this study, the observation of trapped modes around a vertical surface-piercing circular cylinder placed symmetrically within the walls of an open channel was reported. The channel was 12.8 m long and 0.427 m wide; water depth was fixed at 0.7 m. The cylinder was given a step impulse perpendicular to the channel centreplane from an arbitrary rest position and then held with its axis

perpendicular to the waveguide bottom. The transient free-surface disturbance was measured by means of two single-point wave gauges placed symmetrically at either side of the cylinder, on a line perpendicular to the guide walls. Using this set-up, three values of the control parameter (ratio of cylinder radius to waveguide width) were explored, each of which was associated with an NS mode of sharply defined frequency within 0.4 % of the predicted trapped-mode frequency. However, due to the nature of their measuring technique, no information was available on the spatial structure of these modes; therefore, no measure of the degree of localization of the modes could be derived. Moreover, the range of geometries explored precluded the observation of NA-type trapped modes.

The aim of this study is to gain further understanding regarding the occurrence of trapped modes of both NS and NA types, the dependence of their eigenfrequencies with geometry, and the characterization of their detailed spatial structure.

This paper is organized as follows. In the next section, we describe the complete experimental set-up employed in this study, along with the optical profilometric system devised for the measurement of the free-surface deformation (FSD). Section 3 presents the experimental results concerning the detailed spatial structure of the trapped modes. Finally, §4 comprises the analysis and comparison of our experimental results with the theoretical predictions available within the frame of the linear theory.

2. Experimental set-up

In this section, we describe both the experimental set-up and protocol devised for the observation and measurement of the trapped modes' resonances.

Figure 1 shows the whole system schematically. For the purpose of its description, the set-up can be divided into two main parts: the channel itself, in which the trapped modes excitation occurs, and the optical measuring system, located over the channel.

2.1. *Channel*

The waveguide is formed by two vertical walls made of Plexiglas, 60 cm long and 10 cm high, separated by a distance $2d = 10$ cm. A vertical circular cylinder of diameter $2a$ is positioned within the guide. Employing this set-up, two configurations where the obstacle is placed symmetrically between the walls were explored. In the first configuration, the cylinder is located at a distance $3a$ from the entrance (figure $2a$), whereas the second configuration consists of the obstacle centre equidistant from the guide ends (see figure $2b$). For later reference, these two different obstacle configurations will be termed I and II, respectively.

For each one of these two configurations, obstacles of 12 different sizes ($2a = 20$, 30, 40, 50, 60, 70, 75, 80, 85, 90, 95, 100 mm) were employed, keeping the waveguide walls fixed at a distance of $2d = 100$ mm. In every case, the positioning of both the waveguide walls and the cylinder within them were assured to a precision of 0.1 mm. For each of these obstacles, a significant range of frequencies around the theoretical resonance was explored.

The whole waveguide–obstacle system is placed inside a larger water tank of dimensions $60 \times 180 \times 15$ cm³, both the walls' and the obstacle's bases being in contact with the bottom of the tank. Water was employed as the working fluid, keeping a constant level of $\mathcal{H}_0 = (5 \pm 0.05)$ cm throughout the experiments.

Special attention was taken in the design of the wavemaker mechanism so that it would provide a monochromatic sinusoidal movement of the paddle plate. To that end, we designed a bottom-hinged paddle-type wavemaker, with adjustable stroke
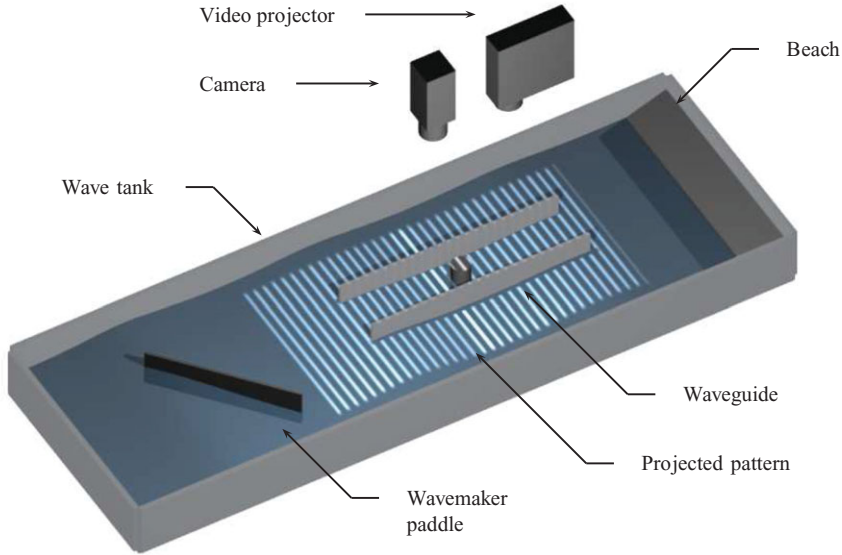
FIGURE 1. (Colour online, available at journals.cambridge.org/flm) Scheme of the complete experimental set-up, depicting both the wave tank and the optical measuring system. Inside the wave tank used for our experiments, the waveguide is placed with its walls parallel to those of the tank. The obstacle is placed symmetrically between the walls of the waveguide, equidistant from the waveguide ends. The wavemaker is positioned near the waveguide, inclined with respect to its entrance in order to excite an asymmetric perturbation within it. At the other side of the wave tank, a sloped beach is used to avoid unwanted wave reflections. Our optical profilometric measuring system is placed over the channel, and is composed of a high-resolution video projector and a high-speed Phantom V9 camera. The video projector projects fringes onto the free surface (shown schematically in the figure) and the camera is used to capture images of the deformed fringes over the region of interest.
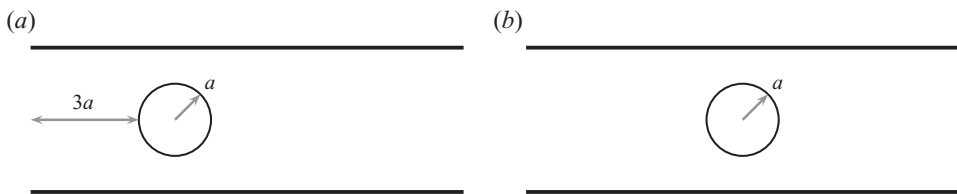

FIGURE 2. Two different obstacle arrangements employed in this study, hereafter termed configurations I (*a*) and II (*b*).

amplitude and servo-controlled forcing frequency in the range of 1–5 Hz, adjustable in 0.02 Hz steps. The inner face of the paddle plate is put in contact with a thin circular disk placed above the water level with its axis perpendicular to the channel bottom. In turn, the disk is attached excentrically to the axis of a rotating motor fixed to the wavemaker structure. Mechanical contact between the paddle and the disk is assured at all times by means of an auxiliary spring system. This way, a constant-speed rotary motion of the motor is transferred by the disk through the contact point to the paddle plate which describes a sinusoidal movement. Prior to this

study, the monochromaticity of the wave paddle was checked measuring the spectrum of its oscillatory motion by laser triangulation. According to that preliminary test, the contribution of the harmonics is approximately four orders of magnitude smaller than that of the fundamental frequency in the energy spectrum, which renders it an efficient monochromatic wavemaker for the purposes of this study.

The key factor for achieving the excitation of trapped modes is to send a small antisymmetric perturbation inside the guide. As theoretically predicted trapped modes are known to be antisymmetric with respect to the waveguide longitudinal centreplane, to be able to excite such trapped modes inside the waveguide, one must be capable of forcing a perturbation with antisymmetric components at the entrance. From an experimental standpoint, two practical limitations are naturally imposed on the amplitude of the antisymmetric perturbation at the entrance of the waveguide. The first constraint is imposed by the presence of dissipation, which demands the perturbation to be large enough at the entrance, so the amplification around the obstacle could be detected by our measuring technique. However, it should also remain small so that the effect of nonlinearities does not become significant. These two constraints led us to a configuration in which the wavemaker is placed at an angle of around $40°$ with respect to the waveguide centreline, so that both antisymmetric as well as symmetric components are transmitted down the guide. It should, however, be noticed that these two components travel differently inside the waveguide. The symmetric part of the perturbation behaves as a propagating wave for any incident frequency, as both ends of the waveguide are open. In contrast, any antisymmetric component with frequencies below the cutoff, $kd < \pi/2$, enters the guide as an evanescent wave.

At the other end of the water tank, $60\,$cm away from the waveguide exit, an inclined beach is disposed in order to mitigate unwanted wave reflections. This wave-absorbing beach is made of a styrofoam-covered rectangular plastic plate and is placed forming an angle of approximately $20°$ with the tank bottom. In spite of its simplicity, preliminary tests showed that the reflected-to-incident wave amplitude ratio was slightly less than $5\,\%$, which renders it a highly efficient absorber for the purposes of this study.

2.2. *Optical measuring system*

A complete characterization of the water-wave trapped-mode resonances requires their observation and localization in frequency space, as well as a detailed study of their global spatial structure and time evolution. In order to pursue such an experimental description, the measuring technique should meet several requirements. The first requirement is that of being non-intrusive, so as not to introduce external perturbations to the system under study. To account for the spatial structure of the surface trapped modes, the technique should be global, i.e. able to measure the FSD over an extended area of the surface. In addition, a high spatial resolution within this interrogation area is demanded so that the smallest significant features of the flow are detected correctly. In our case, this amounts to wavelengths of the order of the capillary length. An additional condition arises from the consideration of the measurement range. In general, resonant states are characterized by amplitudes which considerably exceed those associated with far-off-resonance states (in the particular case of this study, as much as 30 times). Therefore, measuring the FSD amplitude consistently as it approaches the resonant state requires a high vertical resolution throughout a large vertical measurement range. The last major requirement on the measuring technique focuses on its temporal resolution. Indeed, short observation

times are imperative to accurately follow the dynamics of (local) perturbations in their propagation and spread along the surface. Therefore, the propagation velocity of surface waves emerges naturally as a limiting factor which, together with the spatial resolution, sets a threshold for the observation time.

These requirements have led us to the development of an optical profilometric technique that allows for high-resolution three-dimensional whole-field reconstruction of time-dependent FSD fields. Our technique is based on a particular fringe projection profilometry method known as Fourier transform profilometry (hereafter termed FTP), originally due to Takeda, Ina & Kobayashi (1982) and Takeda & Mutoh (1983), successfully applied in the past for the topography of solid surfaces in a variety of fields such as mechanical engineering, machine vision, industry monitoring, quality assessment, etc. The adaptation and enhancement of this particular technique for the measurement of FSDs were described by Cobelli *et al.* (2009) and Maurel *et al.* (2009), where its applicability to a variety of fluid dynamics problems was demonstrated.

The operating principle of the FTP method is the following. A fringe pattern of controlled characteristics is projected onto the free surface and its image is registered by a camera. The deformed fringe pattern due to the surface deformations is later compared to the undeformed (reference) one, leading to a phase map. A phase-to-height relation involving the optical system parameters can be derived based on the laws of geometrical optics, from which the local free-surface height can be reconstructed.

The optical measuring system devised for high-resolution surface deformation mapping is also schematically shown in figure 1. In our experiments, water was employed as the working liquid. In order to be able to project images onto the water surface, its light diffusivity is enhanced by the addition of a white (titanium-dioxide-based) liquid dye. Any potential variation in the surface tension is not expected to affect our results significatively as our experimental parameters place us in the gravity surface waves regime.

A computer-controlled digital video projector with a resolution of $1\,920 \times 1\,280$ pixels^2 and 12 bit depth is employed for the projection of fringe patterns. This allows us to project sinusoidal fringe patterns of controlled wavelength, more adapted to Fourier analysis than the square profile (Ronchi-type) gratings commonly used. This results in an overall quality gain in both the frequency space filtering process inherent to the technique and in the phase recovering. Another advantage of this video projector system is the possibility to laterally shift the projected pattern, displacing it towards the field of view of the camera without introducing optical aberrations that would deform the fringes. Once the projector–free-surface working distance L is set, the size of the projection window can be adjusted to fit either a small or a relatively large area over the liquid surface. In this experimental study, we employed a projection distance $L = 100.7\,\text{cm}$ and a projection window covering (but not limited to) the entire free surface (including the obstacle) within the waveguide, of size $10 \times 40\,\text{cm}^2$.

The fringe patterns projected onto the liquid free surface were recorded by a Phantom V9 monochrome high-speed camera, with a resolution of $1\,632 \times 1\,200$ pixels^2 and a bit depth of 10 bits. The wavelength of the pattern projected onto the free surface was set at $2\,\text{mm}$, which corresponds to 9 pixels in the camera CCD (charge-coupled device). The relative positioning of the video projector and the camera is as follows. Their optical axes are perpendicular to the channel bottom, parallel to one another, and separated by a distance $D = 35\,\text{cm}$. The
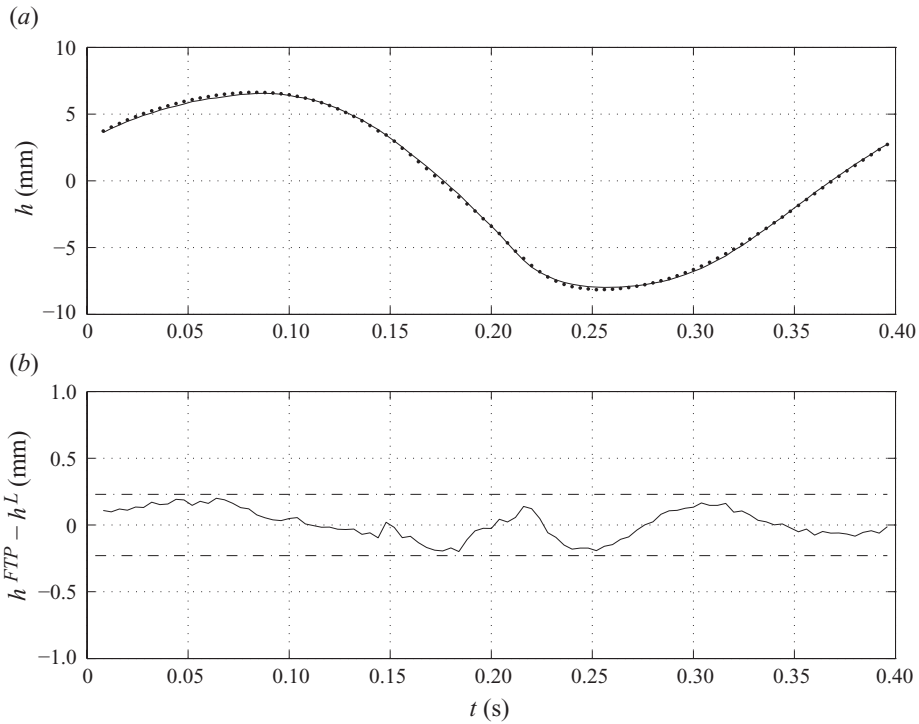
(*a*)

(*b*)

FIGURE 3. Comparison between two measurements made at the same point with a standard laser profilometer (plain line) and FTP at the same point (dashed line). (*b*) Difference between both measurements (FTP and laser profilometry) at the same point.

entrance pupils of both instruments lie on a plane parallel to that of the unperturbed surface, a distance L over it. Data acquired by the camera were later recorded as uncompressed raw tagged image file format (TIFF) to avoid any artefact from the camera firmware preprocessing algorithm, such as those associated to quantization, compression, colour-depth reduction, etc. The whole fringe projection and image capturing system is held over the channel supported by a structure that allows for precise alignment and relative positioning of the optical devices.

This technique has a theoretical resolution in the measured surface elevation given by geometrical optics which is limited by the size of the projected pixel. In the present experiments, the latter corresponds to 0.23 mm. The attained resolution is exemplified in figure 3, where a comparison with a measurement by laser profilometry (5 μm precision) has been performed at a particular point in the surface. In this figure, $|h^{FTP} - h^{laser}| \leqslant 0.2$ mm, in agreement with the estimated resolution. This validates our measurements and fixes the resolution.

2.3. *Data acquisition and treatment*

For any given values of a/d and driving frequency f, the camera sampling frequency f_S was set at $f_S = 100f$, leading to 100 frames per period. Two periods of oscillation were registered in each case. For every image in a time series, a free-surface height is obtained by means of the inversion algorithm used in FTP.

2.3.1. *Decomposition in harmonics of the driving frequency*

The global nature of our measuring technique allows us to decompose the time evolution of the FSD $h_T(x, y, t)$ in terms of the harmonics of the driving angular frequency $\omega = 2\pi f$. The latter can be represented as a complex Fourier series expansion in the following form:

$$h_T(x, y, t) = \mathrm{Re} \sum_{n=0}^{\infty} H_n(x, y)\, \mathrm{e}^{\mathrm{i}\phi_n(x,y)}\, \mathrm{e}^{\mathrm{i}n\omega t}, \qquad (2.1)$$

where we have introduced two real-valued fields: the amplitude $H_n(x, y)$ and phase $\phi(x, y)$ associated with the nth harmonic. The symbol Re denotes, as is customary, the real part of the expression following it. Equation (2.1) can also be expressed as

$$h_T(x, y, t) = \mathrm{Re} \sum_{n=0}^{\infty} h_n(x, y)\, \mathrm{e}^{\mathrm{i}n\omega t}, \qquad (2.2)$$

introducing the complex-valued amplitude $h_n(x, y)$ given its magnitude $H_n(x, y)$ and its phase $\phi_n(x, y)$ through

$$h_n(x, y) = H_n(x, y)\, \exp\{\mathrm{i}\phi_n(x, y)\}. \qquad (2.3)$$

To achieve such a decomposition, the coefficients of the Fourier expansion in time are calculated at each measurement point (x, y) over the measured region of the free surface (employing 100 frames per period, which allows for an accurate integration).

Such a decomposition scheme in terms of harmonics of the driving frequency presents many advantages for the analysis of the dynamics of the FSD. On the one hand, separation of the linear part of the FSD from the nonlinear contributions (with frequencies corresponding to 0, 2ω, 3ω, etc.) is straightforward, which enables a comparison between the two. Furthermore, when complemented by the global nature of our measuring technique, this comparison serves to evaluate the relative importance of the nonlinear components *locally* within the guide. In the case of this experimental study, this separation is particularly suitable as it allows us to precisely compare our results with the predictions from the available *linear* theories (see §4).

2.3.2. *Decomposition in symmetric and antisymmetric parts*

Finally, we define two fields, one symmetric and another antisymmetric about the waveguide centreline by means of the usual definitions

$$h_n^s(x, y) = \tfrac{1}{2}[h_n(x, y) + h_n(x, -y)], \qquad (2.4)$$

$$h_n^a(x, y) = \tfrac{1}{2}[h_n(x, y) - h_n(x, -y)], \qquad (2.5)$$

for the symmetric and antisymmetric parts, respectively.

3. Resulting patterns

In this section, we expose the results obtained following the previously described decomposition from the instantaneous total fields to the harmonics and finally to the symmetric and antisymmetric fields. The latter antisymmetric field corresponds to the trapped mode that is the main subject of this study.

3.1. *Instantaneous free-surface deformation field*

Figure 4 shows a sequence of instantaneous FSD fields for $a/d = 0.5$ and $f = 2.5$ Hz, close to the experimentally determined resonant frequency (see also Movie 1,
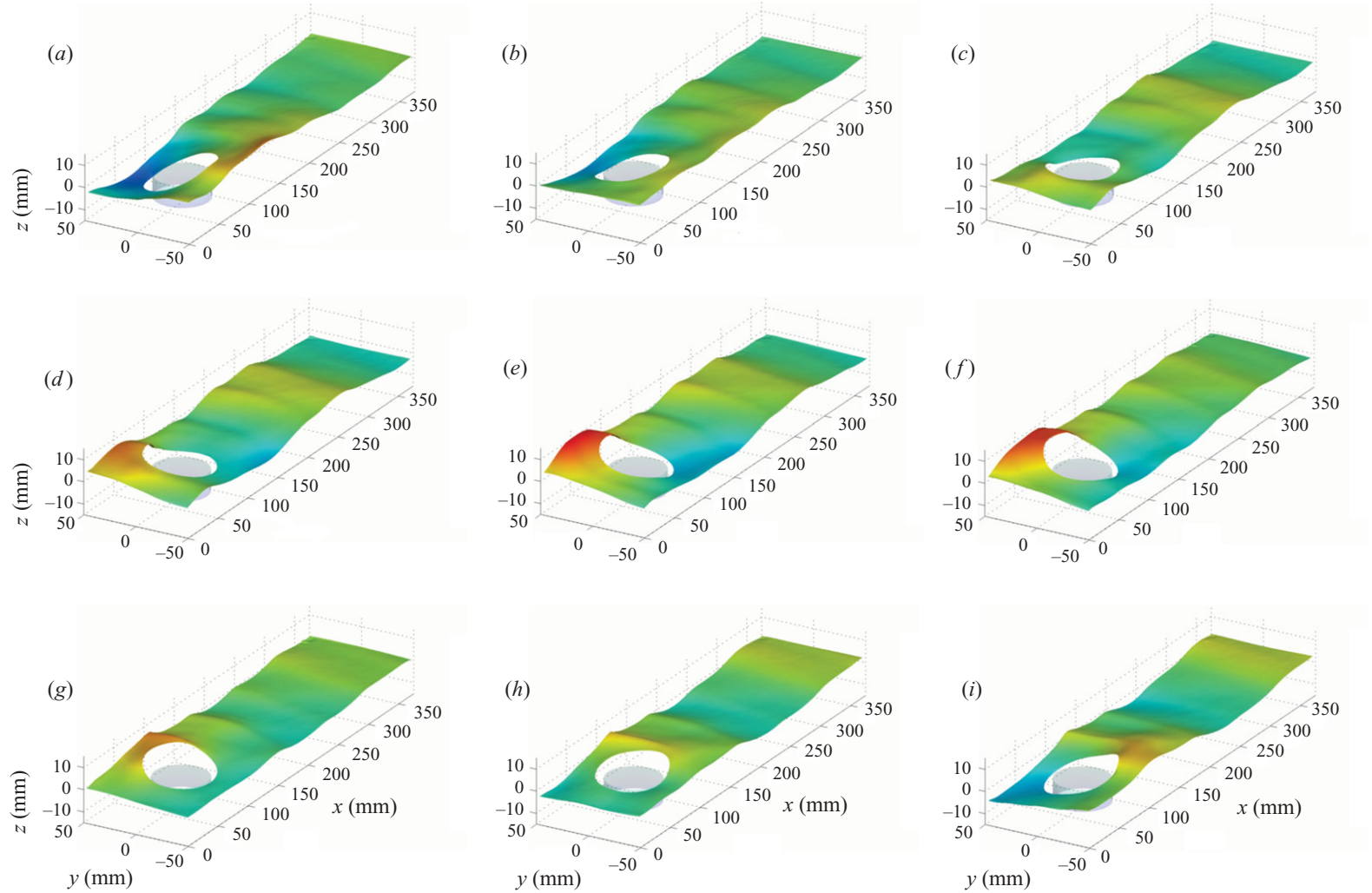
FIGURE 4. Experimental measurements of the instantaneous total FSD fields. The figure shows a time sequence of the evolution of the FSD fields for a particular case of the aspect ratio explored, namely $a/d = 0.5$. The wave incident frequency corresponds to $f = 2.5$ Hz. The plots represent successive time steps of 0.1 times the period. (Spatial (in-plane) and vertical resolutions are Δx, Δy, $\Delta z = 0.2$ mm.) For reference, the obstacle is schematically depicted in this snapshot by the inclusion of a semi-transparent truncated cylinder.

FIGURE 5. Example view of the free surface as seen by the camera, for $a/d = 0.5$. The image shows the presence of shadows and bright spots in the vicinity of the cylinder, precluding profilometric measurements in that region. The elliptical boundary of this region is shown in black in this picture. The linear colourmap depicts the light intensity over the surface in normalized units.

available at journals.cambridge.org/flm). In practice, this sequence consists of 100 frames registered at an acquisition rate of 250 Hz. Here, only 1 over 10 fields is shown. For the present figures, configuration II was chosen because the cylinder being closer to the entrance makes the amplitudes larger, rendering the phenomenon more evident. In these figures, local height is linearly colour-coded between red and blue, the former corresponding to elevations and the latter to depressions with respect to the free surface at rest. With this convention, green is associated with undeformed regions. For the sake of comparison, the same colour scale was maintained throughout the sequence.

Although the measurement region includes the whole free-surface area within the guide, the reconstruction presents a dead zone that extends a few millimetres from the obstacle boundary into the fluid. The presence of this zone in our reconstructions is due to the relative positioning of the video projector source and the cylinder. Figure 5 shows the region of interest of the free surface within the waveguide, as seen by the camera. At the front of the cylinder (facing incident waves), there is a region of the surface that is in shadows, and from which no information about the local fringe deformation is available. At the rear, a specular reflection of the projecting source on the wall of the cylinder introduces a bright spot on the surface, with similar implications. Therefore, in the reconstructions, these zones are hidden by a mask larger than the obstacle. The same is true for a thin layer near the walls (~ 2 mm) which are not accessible for measurement due to the presence of a reflection of the projector source.

The snapshots in figure 4 illustrate the dynamics of the free surface in the presence of a trapped mode. The region near the obstacle is characterized by an asymmetric oscillation at the driving frequency, with large amplitudes. In this region, the local surface curvature is rather large, as evidenced by the presence of steep slopes in the vicinity of the obstacle.

In contrast, the region far past the cylinder mainly shows the propagation of a plane, slightly attenuated wave. Furthermore, the amplitude of this wave is of the same order as that of the incident wavefront. Perhaps the most striking feature observed in this region is the recovery of symmetry.

These observations effectively suggest the existence of an antisymmetric deformation localized in the vicinity of the obstacle, decaying rapidly with distance. However, and due to our particular choice of the experimental set-up, the theoretically predicted
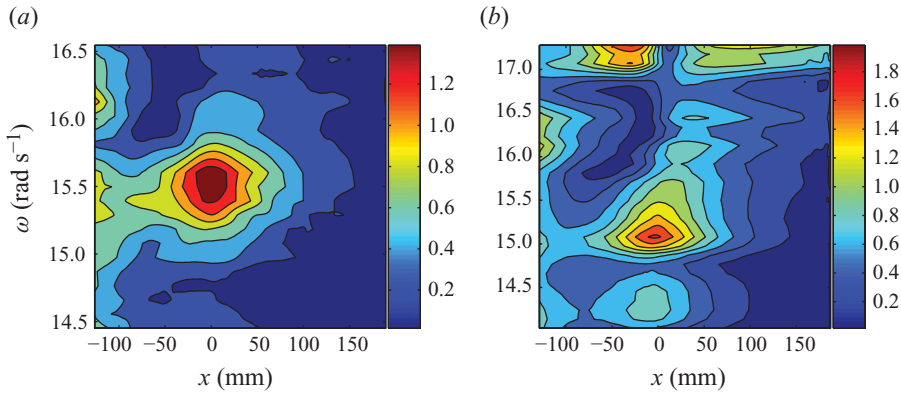
FIGURE 6. Experimental evidence of the trapped-mode resonance: $(1/2)\max_t|h_T(x, y_0, t) - h_T(x, -y_0, t)|$ at a fixed y_0 is displayed in colour scale as a function of x and ω. (*a*) For $a/d = 0.5$, one resonance is visible near the cylinder; (*b*) for $a/d = 0.85$, in addition to the first resonance, a second maximum near the cutoff angular frequency can be seen. The cylinder lays at $x = 0$ mm (configuration I). The scale of the colour bar is in millimetres.

pure antisymmetric nature of the trapped mode is still concealed by the plane wave propagating down the waveguide and by the presence of nonlinearities (if any).

From these acquisitions, a direct but qualitative evidence of the trapped-mode resonance can be exhibited. The symmetry of the geometry decouples the fields into two families, even and odd with respect to y. Figure 6 shows the odd part: $(1/2)\max_t|h_T(x, y_0, t) - h_T(x, -y_0, t)|$ as a function of both x and the driving pulsation ω at a fixed y_0. One or two spots with maximum amplitudes are visible in the vicinity of the cylinder at some particular angular frequencies, indicative of the presence of resonances.

3.2. *Pattern of the harmonics*

A time decomposition in harmonics of the driving frequency is calculated from 100 instantaneous FSD fields within one period. It is worth noting that for such a decomposition of the *instantaneous* FSD fields, the time instant $t = 0$ s corresponds to a fixed phase of the wavemaker, chosen as to coincide with the endpoint of its forward stroke.

The first three Fourier modes obtained with this decomposition ($a/d = 0.5$, at the resonance frequency $f_r = 2.47$ Hz) are shown in figures 7 and 8 for type I and type II configurations, respectively. These first three components represent 98 % of the total FSD, higher order harmonics being negligible.

For both types of configurations (figures 7 and 8), the linear mode $h_1(x, y, t)$ is depicted in panel (*b*). Type I configuration clearly shows a stronger resonance than type II configuration. Indeed, the larger the amplitude of the incident antisymmetric wave, the larger the amplitude of the trapped mode. In configuration I, where the cylinder is close to the entrance, the antisymmetric part of the incident wave is larger when reaching the cylinder than in the case of the second configuration, in which the amplitude of the antisymmetric part of the wave reaching the cylinder is much more attenuated due to its evanescent nature.

Panels (*a*) and (*c*) show the first two nonlinear fields $h_0(x, y)$ and $h_2(x, y, t)$ at 0 and 2ω, respectively. The zeroth-order contribution, $h_0(x, y)$ shown in figures 7(*a*) and 8(*a*), also represents the first nonlinearity of the deformation field, at the same
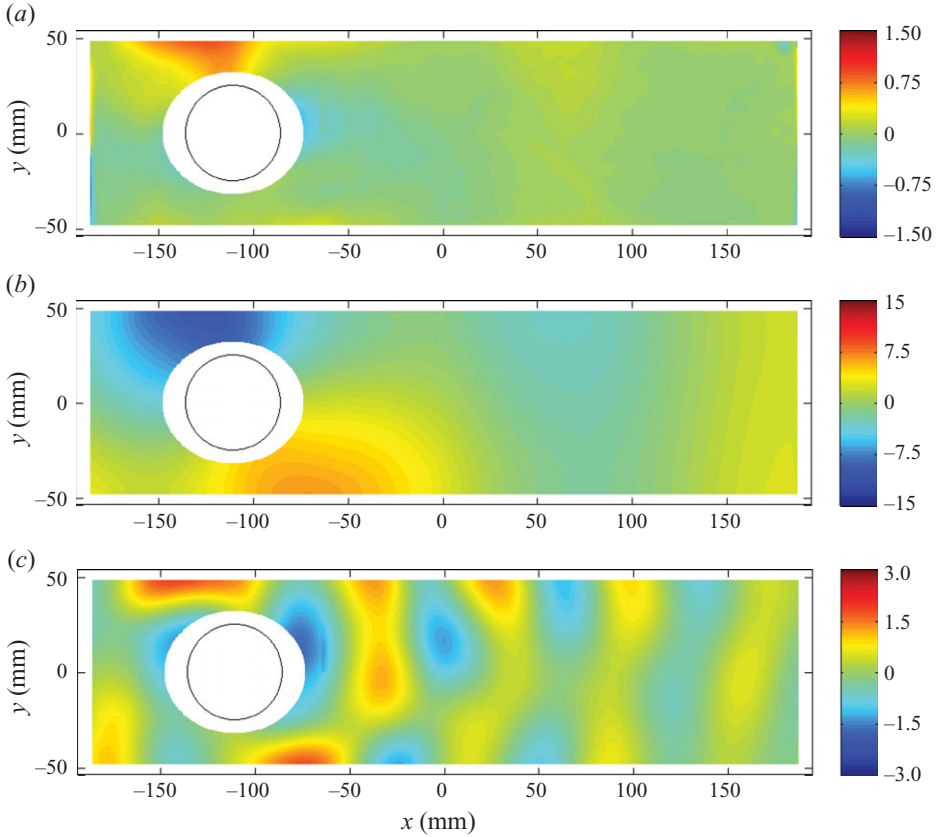
FIGURE 7. Experimentally measured FSD fields decomposed in harmonics of the driving frequency: type I configuration for $a/d = 0.5$. (a) Zeroth harmonic $h_0(x, y)$, (b) linear contribution $h_1(x, y, t)$ and (c) second harmonic component $h_2(x, y, t)$ corresponding to a pulsating frequency of 2ω. The position of the obstacle within the waveguide is indicated by the black circle. The scale of the colourbar is in millimetres.

level as the more classically known first harmonic (at 2ω). It corresponds to the local steady deformation of the free surface, representing a distortion to the base flow. This zeroth harmonic, being a stationary nonlinearity, is of particular interest in the study of flow control for instance (Maurel, Pagneux & Wesfreid 1995; Protas & Wesfreid 2002).

The field $h_2(x, y, t)$ corresponds to oscillations of twice the pulsation frequency. It is mainly located around the cylinder in configuration I, and at the entrance of the waveguide in configuration II. In each case, this corresponds to the maximum amplitude of the linear field. The zeroth and first harmonics present amplitudes which are of order 10 % and 20 %, respectively, of the amplitude corresponding to the linear contribution in the first configuration, whereas in the second configuration considered, they represent only 1 % and 5 %. From this observation, we expect the first configuration to be considerably more nonlinear than the second one.

The decomposition in harmonics of the driving frequency that we have shown so far admits a complementary representation in terms of the amplitudes $H_n(x, y)$ and phases $\phi_n(x, y)$ of the FSD, as described in (2.1). Figure 9 illustrates the outcome of
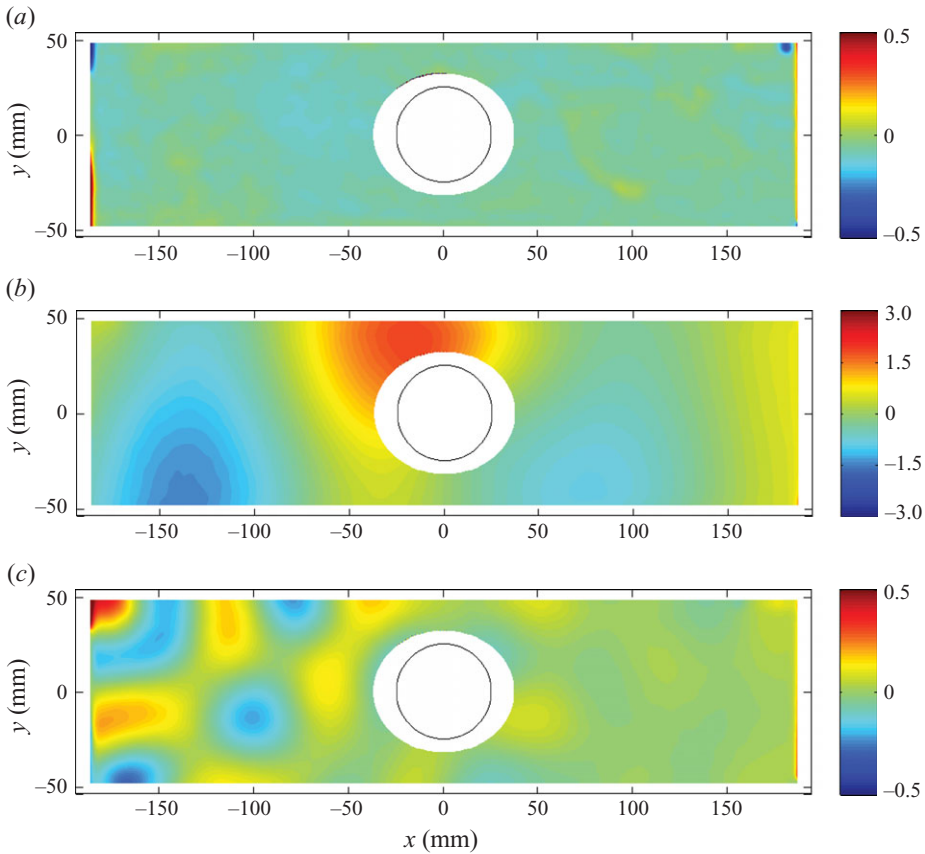
FIGURE 8. Experimentally measured FSD fields decomposed in harmonics of the driving frequency: type II configuration for $a/d = 0.5$. (*a*) Zeroth harmonic $h_0(x, y)$, (*b*) linear contribution $h_1(x, y, t)$ and (*c*) second harmonic component $h_2(x, y, t)$ corresponding to a pulsating frequency of 2ω. The position of the obstacle within the waveguide is indicated by the black circle. The scale of the colourbar is in millimetres.

such a decomposition in terms of amplitudes and phases. For this figure, we have considered the experimental results for $a/d = 0.5$ at the resonance frequency, in the case of type I configuration (cylinder closer to the waveguide entrance).

Panel (*a*) on top of the figure depicts $H_0(x, y)$, the amplitude corresponding to the zeroth-order harmonic. At the centre of the figure, panel (*b*) shows the linear mode amplitude, $H_1(x, y)$ (on the left) and its phase $\phi_1(x, y)$ (on the right). Finally, the second harmonic is presented in panel (*c*), showing $H_2(x, y)$ (on the left) as well as its phase $\phi_2(x, y)$ (on the right).

The relative contribution of each of these modes to the total FSD can also be assessed by comparing the amplitudes in the left column, an analysis that has already been discussed in the previous section (figures 7 and 8).

The phase of the linear contribution (figure 9*b*) shows, as expected, a phase jump around the cylinder. An interesting feature is to detect a second phase jump of opposite sign which allows the recovery of a plane symmetric wave downstream. This second phase jump appears as a singularity that is associated to a point with zero amplitude. It is worth noting that this would not have been detected in standard
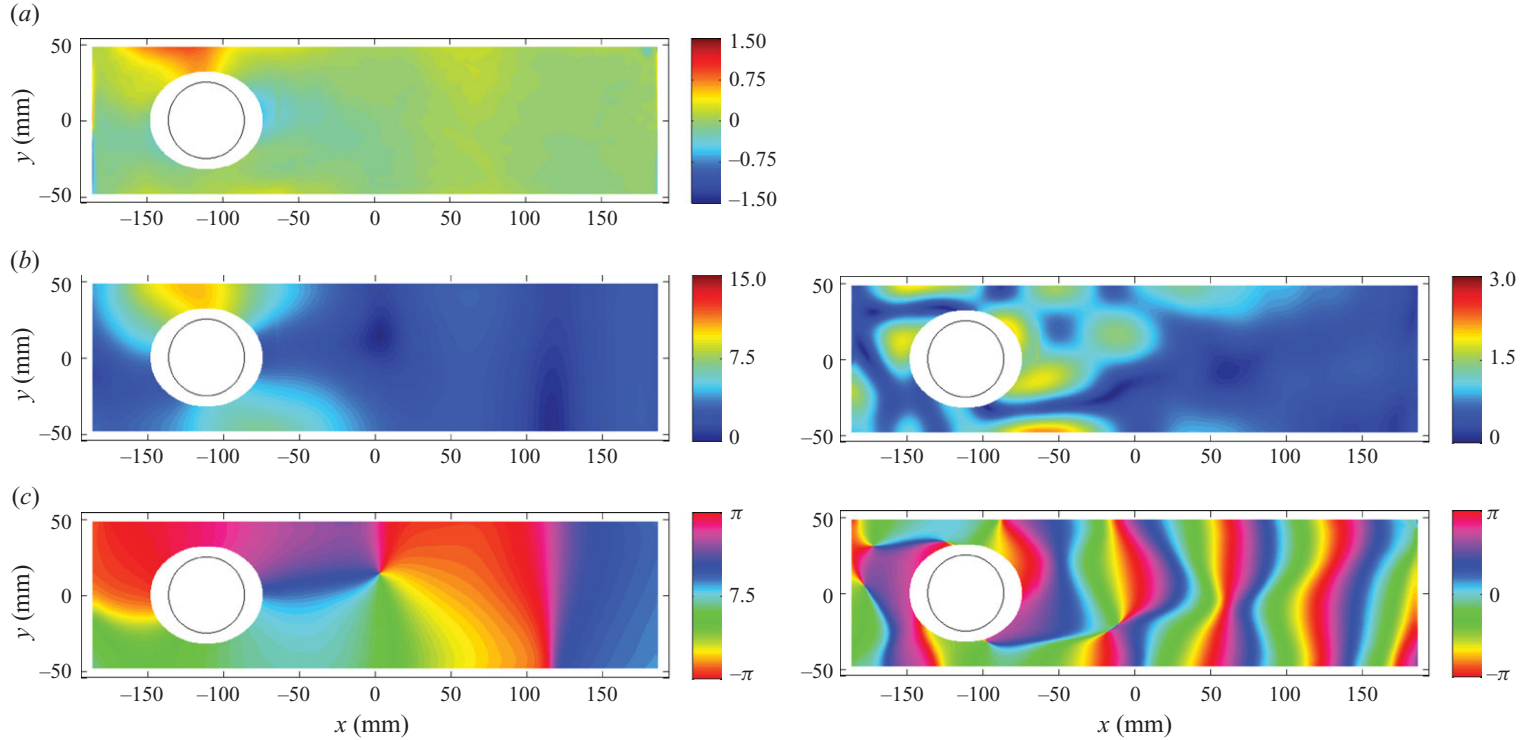
FIGURE 9. Experimental results for the decomposition of the total deformation field in harmonics of the driving frequency: type I configuration for $a/d = 0.5$. Representation in amplitude and phase. (a) Zeroth Fourier mode $H_0(x, y)$, (b) linear contribution $H_1(x, y)$ and (c) second harmonic component $H_2(x, y)$ corresponding to a pulsating frequency of 2ω. The position of the obstacle within the waveguide is indicated by the black circle. For the amplitudes, the scale of the colourbar is in millimetres. Phase values are contained in the interval $[-\pi, \pi]$.
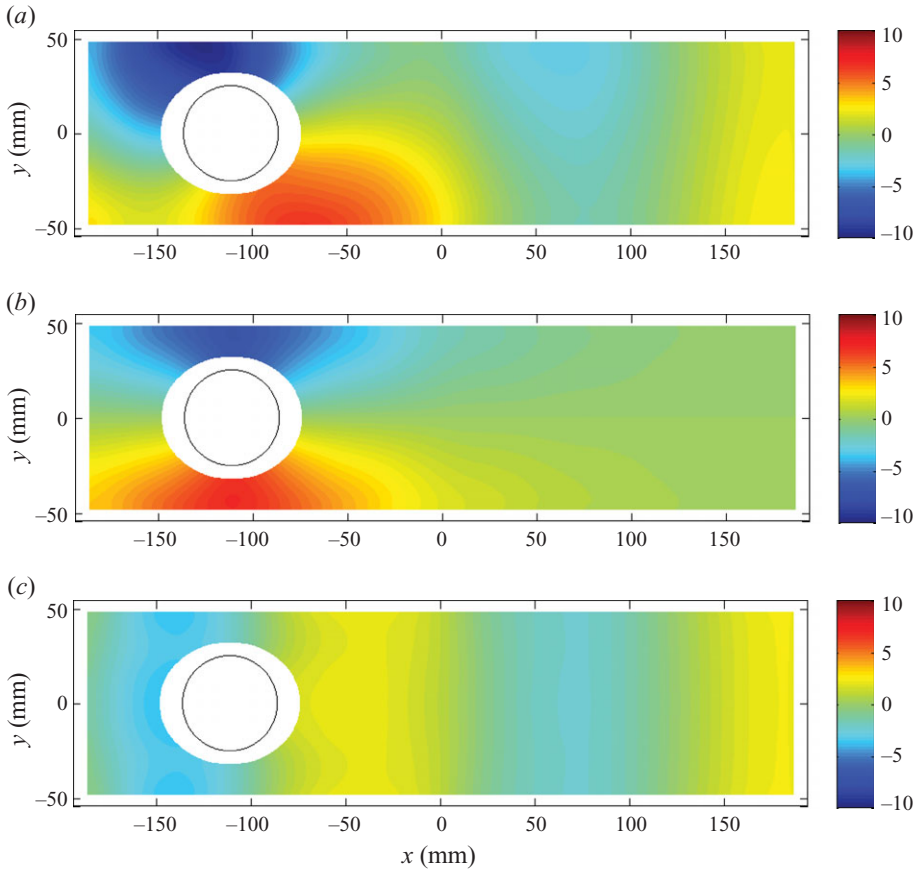
FIGURE 10. Linear part of the experimentally measured FSD: type I configuration for $a/d = 0.5$. Panel (*a*) shows the linear deformation field $h_1(x, y)$ (same as in figure 7*b*). Panels (*b*) and (*c*) presents the antisymmetric and symmetric parts of the linear mode $h_1(x, y)$, respectively. The position of the obstacle within the waveguide is indicated by the black circle. The scale of the colourbar is in millimetres.

single-point measurement experiments, where such a decomposition in terms of the harmonics of the driving frequency is not available. (Movie 2 shows the amplitude in time around this point singularity, both in the total and linear part of the field.)

3.3. *Trapped-mode pattern*

The detailed spatial structure of the trapped modes can be obtained from the linear deformation fields by a separation in terms of the natural symmetries of the problem. Figures 10 and 11 illustrate the results of such a decomposition for the case of $a/d = 0.5$ at the trapped modes' resonance frequency, in type I and type II geometrical configurations, respectively. Panels (*a*) show the linear part of the deformation fields, (same as figures 7*b* and 8*b*, reproduced here for clarity), whereas panels (*b*) and (*c*), respectively, depict its antisymmetric and symmetric parts.

We observe that the antisymmetric part of the field is symmetric with respect to the Oy axis in this linear contribution. Comparing panels (*b*) and (*c*) in figure 10, it is evident that, in this case, the trapped mode dominates the dynamics of the free surface, with a maximum amplitude which is approximately four times that of its
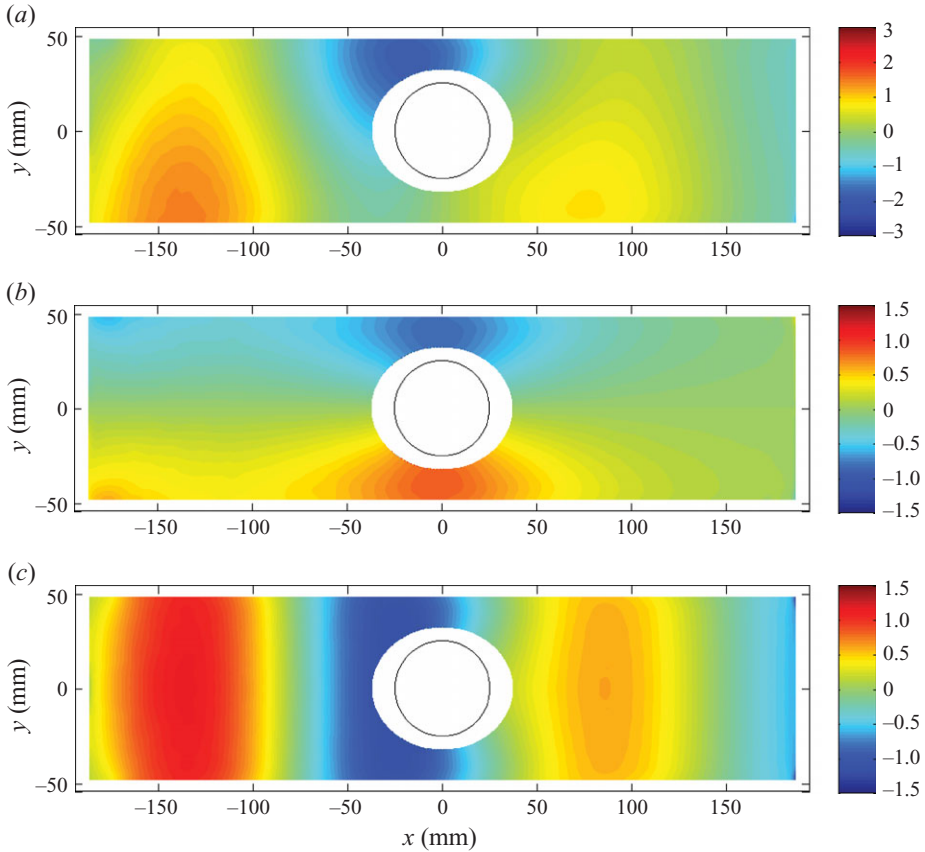
FIGURE 11. Linear part of the experimentally measured FSD: type II configuration for $a/d = 0.5$. Panel (*a*) shows the linear deformation field $h_1(x, y)$ (same as in figure 8*b*). Panels (*b*) and (*c*) present the antisymmetric and symmetric parts of the linear mode $h_1(x, y)$, respectively. The position of the obstacle within the waveguide is indicated by the black circle. The scale of the colourbar is in millimetres.

symmetric counterpart. In contrast, figure 11 shows that, in the latter case, both the symmetric and antisymmetric parts contribute in essentially the same amount to the total linear FSD.

Moreover, and even though they do not share the same scales, comparison of panels (*b*) in figures 10 and 11 shows that, in both cases, i.e. either for the obstacle placed near the entrance of the waveguide or at its centre, the spatial structure of the trapped modes is qualitatively similar.

In figure 10(*b*), the amplitude near the cylinder is of order 10 mm, in the case considered here. This amplitude would have been of order ~ 0.2 mm in the absence of the cylinder. In figure 11(*b*), where the cylinder is further down the guide, the amplitude of the antisymmetric part is of order 1 mm, compared to the value that would have been of order 0.02 mm in the absence of the cylinder. As will be shown later (see figure 15), the amplitude of the antisymmetric mode decreases exponentially because of the evanescent nature of this mode. Knowing α, the value of the amplitude in absence of the cylinder is calculated as $A_0 e^{-\alpha D}$, where A_0 is the amplitude at the entrance of the waveguide and D the distance of the cylinder centre to the guide entrance.
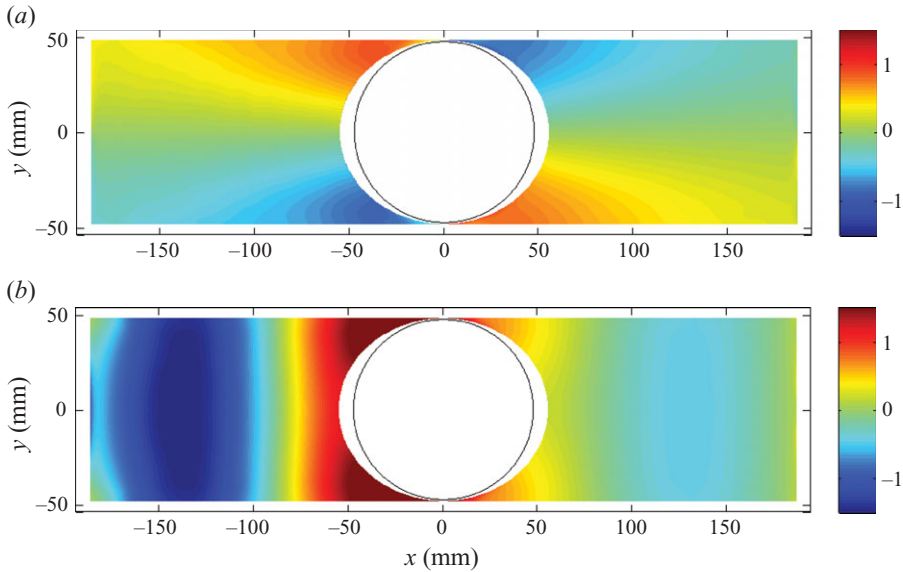
FIGURE 12. Experimental pattern of an NA-trapped mode. (*a* and *b*) Antisymmetric and symmetric fields (respectively) of $h_1(x, y, t)$ for $a/d = 0.95$ and $kd = 1.51$ ($f = 2.62$ Hz). The position of the obstacle is indicated by the black circle. The scale of the colourbar is in millimetres.

The symmetric part (figures 10*c* and 11*c*) shows a plane wave that is slightly attenuated in amplitude as it propagates down the guide. Incidentally, symmetric patterns are used to obtain a direct measurement of the incident wavenumber k (see §4.1).

Figure 12 shows the experimental pattern of the NA-trapped mode associated to the aspect ratio $a/d = 0.95$, at the frequency $f = 2.62$ Hz (corresponding to $kd = 1.51$). The panels (*a* and *b*) in this figure depict the antisymmetric and symmetric fields of the linear contribution $h_1(x, y, t)$, respectively. The antisymmetry of the deformation field in panel (*a*) is striking, particularly in view of the two small gaps connecting the two sides of the obstacle, of size 2.5 mm. Such NA-trapped modes were observed in the experiments for the largest aspect ratios considered, namely for $a/d = 0.85, 0.9$ and 0.95, in agreement with the theoretical predictions given by Evans & Porter (1999).

In the following, we will focus on type II configuration, in which the cylinder is centred longitudinally within the guide. This is done in order to be placed in the linear regime, avoiding the possible influence of nonlinearities on the linear contribution. In §4.2, the comparison between the spatial structure of the experimentally determined trapped mode $h_1^a(x, y, t)$ and theoretical predictions will be shown.

4. Analysis of the experimental results and comparison with the linear theory

A theoretical description of this problem can be carried out in the framework of linear-wave theory, by means of a velocity potential description, in which $\boldsymbol{u} = \nabla \Phi$. Within this approximation, the velocity potential satisfies the Laplace equation in the fluid

$$\nabla^2 \Phi(x, y, z, t) = 0. \tag{4.1}$$

Separation of the depth dependence leads to a solution of the form

$$\Phi(x, y, z, t) = \phi(x, y) \cosh k (z + \mathcal{H}_0) \, \mathrm{e}^{-\mathrm{i}\omega t}, \tag{4.2}$$

where ω and k are related by the dispersion relation

$$\omega^2 = gk \, \tanh k\mathcal{H}_0, \tag{4.3}$$

where $g = 9.81 \, \mathrm{m \, s^{-2}}$ is the acceleration due to gravity and $\mathcal{H}_0$ is the height of the liquid layer at rest.

The potential $\phi(x, y)$ therefore satisfies the Helmholtz equation in the fluid region,

$$\left(\nabla^2 + k^2\right) \phi(x, y) = 0, \quad \text{in} \quad r > a, \quad |y| \leqslant d, \quad r = \sqrt{x^2 + y^2}, \tag{4.4}$$

subject to Neumann (no-flow) boundary conditions on the walls as well as at the boundary of the obstacle,

$$\partial_y \phi(x, y) = 0, \quad y = \pm d, \quad -\infty < x < \infty, \tag{4.5}$$

$$\partial_r \phi(x, y) = 0, \quad r = a. \tag{4.6}$$

Furthermore, trapped modes are known to satisfy two other conditions. The first one corresponds to their antisymmetric nature (with respect to the centreline of the channel), which can be stated as

$$\phi = 0, \quad y = 0, \quad |x| \geqslant a. \tag{4.7}$$

The second condition is that they should be effectively confined to the vicinity of the cylinder, so that there could be no radiation at infinity,

$$\phi \to 0, \quad x \to \pm\infty, \quad |y| \leqslant d. \tag{4.8}$$

The height of the free-surface perturbation is proportional to the vertical velocity of the surface and the boundary condition on ϕ are imposed on vertically invariant surfaces. We can thus deduce that the height is subject to the same equations and boundary conditions as described in (4.4)–(4.8).

In this section, we will keep only the linear contribution to the FSD, discarding higher order harmonics. Such a treatment in terms of the linear part is justified by the fact that, as was shown in the previous section, the linear contribution effectively dominates, especially in the case where the cylinder is centred in the waveguide (type II configuration). Indeed, experimental evidence on the preponderance of the linear contribution, emphasized in figure 8, has shown that, in this example, the linear part represents 94 % of the total FSD. In turn, this justifies a description of the trapped-mode resonance phenomena in terms of a linear theory and will allow us to compare our experimental results with the available theoretical predictions.

4.1. *Dispersion relation*

From the symmetric part of the field at the driving frequency (as shown in panels (*c*) of figures 10 and 11 and in panel (*b*) of figure 12), we get a direct measurement of the wavenumber k. Although there is only few wavelengths in the waveguide, a reasonable estimate is possible by determining the periodicity of the quantity $h_1^s \times h_1^{s*} \propto a + b \cos 2kx$. Figure 13 shows the result for all values of the a/d ratio
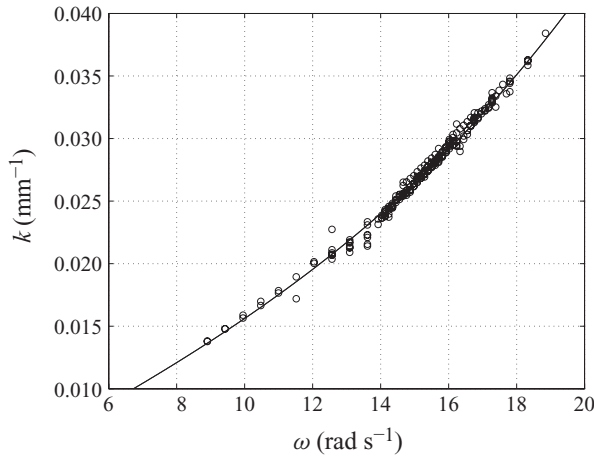
FIGURE 13. Dispersion relation. The point cloud gathers all experimental data points obtained throughout the experiments. The theoretical dispersion relation given by (4.3), represented by the continuous line, is shown for comparison purposes.

considered in this study. The resulting values agree with the theoretical prediction given by (4.3).

As stated previously, the symmetric propagating mode experiences attenuation, which can be represented by assuming a complex valued wavenumber. In the cases where attenuation is accounted for, we use the identification $k \to k + i\epsilon(k)$, where k is real and $\epsilon(k)$ stands for the attenuation due to dissipative mechanisms. Because of the smallness of this attenuation, we have not been able to obtain it from a direct measurement. In contrast, such a determination was made roughly indirectly (see §4.3.2).

4.2. *Analysis of the spatial structure of the trapped mode*

In this section, the detailed spatial structure of the measured surface-wave trapped mode is compared to the theoretical predictions based on multipole expansions (Linton & McIver 2001). In this approach, the FSD is represented by a sum of singularities placed within any structures that are present. These singularities, called multipoles, are constructed in such a way as to satisfy the field equation, the free-surface and bed boundary conditions, and a radiation condition. A linear combination of these multipoles is then considered and made to satisfy the appropriate body boundary condition. This leads to an infinite system of linear algebraic equations for the unknown coefficients of the multipole expansion which can be solved numerically by truncation. In addition, many theoretical studies have shown (e.g. Callan *et al.* 1991) that the systems of equations that result from using a multipole method possess good convergence characteristics and only a few equations are needed to obtain an accurate numerical approximation.

For the case of a surface-piercing vertical circular cylinder placed symmetrically between the walls of an infinite waveguide, we have used the results of the multipole expansion given by Callan *et al.* (1991), $h(r, \theta)$ being φ in their equation (2.11).

A comparison between our experimental measurements and the theoretical predictions of linear theory for three different obstacle sizes is shown in figure 14. In order to establish such a comparison, both the experimental values and the
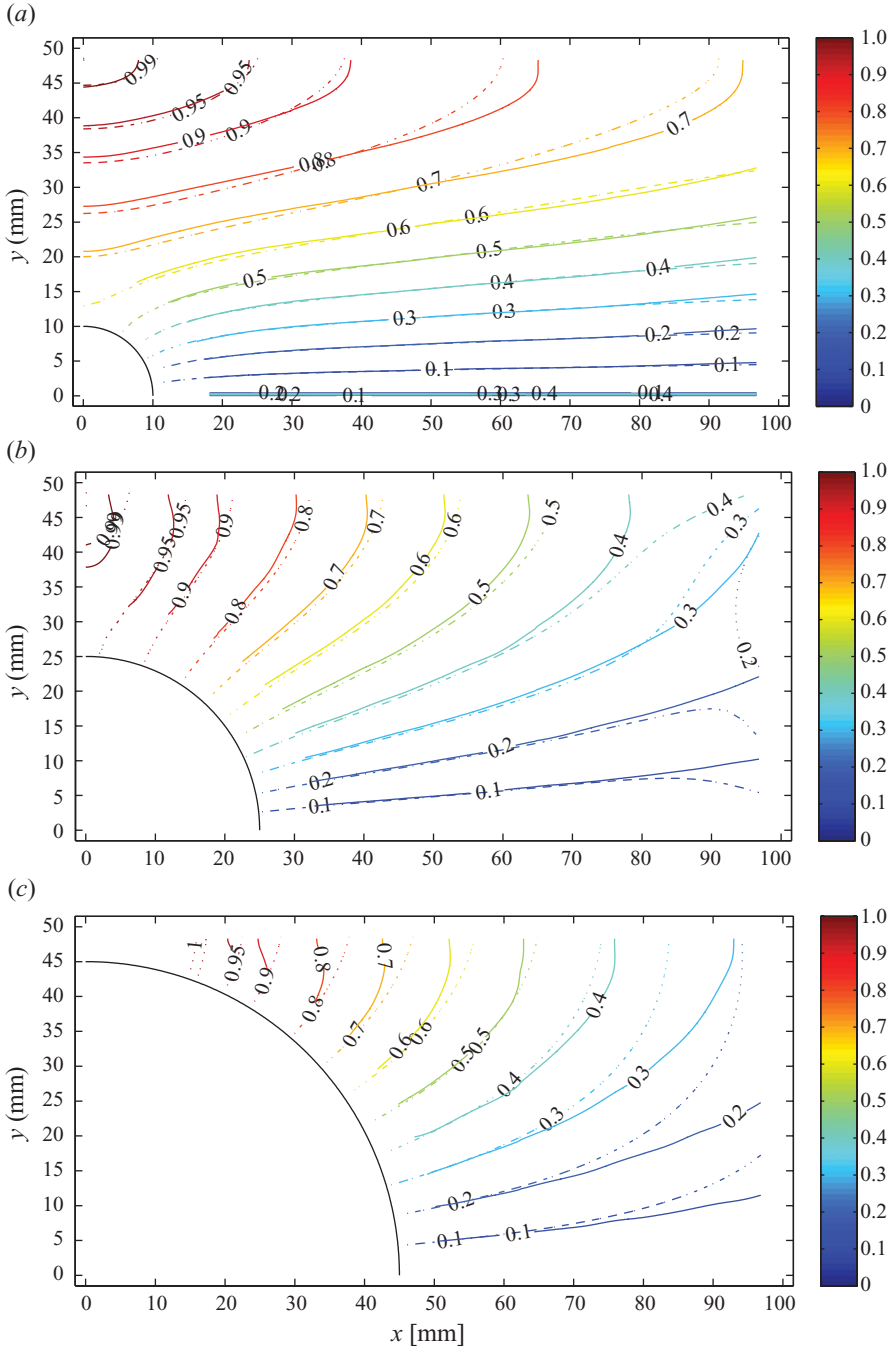
FIGURE 14. (Colour online) Experimentally measured trapped modes' spatial structure as compared to the theoretical predictions from linear theory. Experimental measurements (continuous lines) and theoretical predictions (dashed lines) for three a/d ratios at their respective resonance frequency. (a) $a/d = 0.2$, $kd = 1.55$; (b) $a/d = 0.5$, $kd = 1.39$; and (c) $a/d = 0.9$, $kd = 1.33$. Theoretical and experimental cases are normalized in this case to facilitate the comparison.

theoretical modes (which are solutions of a homogeneous boundary-value problem) are normalized by imposing the value 1.0 on the wall at $x = 0$.

Panel (*a*) corresponds to $a/d = 0.2$, $kd = 1.55$. The theoretical contours depicted in this panel were built using only two multipoles, which assures an error less than 5 %. This figure shows a remarkable agreement between theory and experiment.

The same comparison is presented in panel (*b*) for an intermediate case, namely $a/d = 0.5$, $kd = 1.39$. The theoretical contours to which our experimental data are compared were built using a multipole expansion composed of $N = 6$ multipoles. The agreement between theory and experimental data is very good in the region near the obstacle, and slightly differs far from it. Another source of difference between the two can be found at the walls, as the theoretical model does not take into account the presence of the meniscus that is probably of relevance in the experimental case. Finally, panel (*c*) shows a third case corresponding to $a/d = 0.9$, $kd = 1.33$. Theoretical contours used for comparison in this case correspond to an expansion built using $N = 9$ multipoles. The overall agreement is good.

4.3. *Resonance curves*

4.3.1. *Analysis of the far field: the scattering problem*

The process of excitation of the trapped mode can be analysed as follows. Initially, an antisymmetric wave of amplitude A is sent into the guide. As the associated wavenumber is below the threshold for propagation, the antisymmetric wave enters the guide as an evanescent wave, its amplitude decaying exponentially with distance from the waveguide entrance. However, the presence of an obstacle (placed at a finite distance within the guide) introduces a change in the geometry, drastically affecting the propagation conditions in its vicinity. In that region, even though its amplitude is weak, the incident antisymmetric wave interacts with the obstacle.

This interaction gives rise to a reflection and a transmission of the incident evanescent wave from the obstacle. At the waveguide's exit, there is also a reflection due to the unmatched impedance. The long distance between the obstacle and the exit makes the latter reflection negligible.

Because of the Neumann boundary condition on the waveguide walls, the antisymmetric field can be represented as an infinite linear combination of transverse modes of the form

$$h_1^a(x, y) = \sum_{n=1}^{\infty} H_n \, e^{-\alpha_n |x|} \, \sin(2n - 1) \frac{\pi y}{2d}. \tag{4.9}$$

Each of these transverse modes is associated with an eigenvalue α_n, given by

$$\alpha_n^2 = \left[\frac{(2n - 1)\pi}{2d} \right]^2 - k^2. \tag{4.10}$$

Again, as we are working below the cutoff $(k < \pi/(2d))$, all α_n are real, i.e. every term in (4.9) represents an evanescent mode. Among these, the least evanescent one corresponds to $n = 1$, whose value is simply

$$\alpha \equiv \alpha_1 = \sqrt{\left(\frac{\pi}{2d} \right)^2 - k^2}. \tag{4.11}$$

To go further in our analysis, it is of interest to consider the field $h_1^a(x, y)$ as in a one-dimensional problem by projecting the two-dimensional field onto this dominant
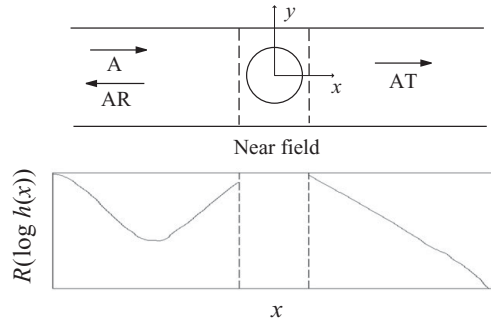
FIGURE 15. (*a*) The problem reduces to a one-dimensional problem along the *x*-axis, by projecting the antisymmetric field onto the first transverse mode in $\sin \pi y / 2d$ outside the near-field region. (*b*) Typical variation of $h(x)$ along the *x*-axis: real part of $\log[h(x)]$ as a function of *x* (a.u.). (The curve has been obtained experimentally for $a/d = 0.4$, $kd = 1.47$.)

first transverse mode. Assuming that

$$h_1^a(x, y) \sim h(x) \sin \frac{\pi y}{2d}, \tag{4.12}$$

the one-dimensional field $h(x)$ is

$$h(x) = \frac{1}{d} \int_{-d}^{d} h_1^a(x, y) \sin \frac{\pi y}{2d} \, \mathrm{d}y. \tag{4.13}$$

As stated before, this assumption is expected to hold only in the far field of the obstacle (see figure 15). In the near-field region, the higher transverse modes are expected to contribute to the two-dimensional solution. The typical behaviour of $h(x)$ is illustrated in figure 15. For the sake of simplicity, the far field can be decomposed into two regions. The first one shows, as expected, the incident evanescent mode whose amplitude decays as it enters the guide as well as its reflection due to the presence of the obstacle. On the other side, only a transmitted mode is found, which rapidly decays away from the obstacle. It is worth noting that, in this case, no reflection is observed from the waveguide exit, which confirms our working hypothesis.

4.3.2. *Shape of the resonance curves*

In the following, we denote by (R, T) the reflection and transmission coefficients of the obstacle, respectively. These magnitudes are of interest as they completely characterize the obstacle as a scatterer, independently of the incident amplitudes which may, experimentally, vary with frequency.

According to the results shown in figure 15, the one-dimensional profile for $h(x)$ in the far field can be represented as a piecewise function, namely

$$h(x) = \begin{cases} A \, \mathrm{e}^{-\alpha x} + AR \, \mathrm{e}^{\alpha x}, & x < 0 \quad \text{(region I)}, \\ AT \, \mathrm{e}^{-\alpha x}, & x > 0 \quad \text{(region II)}, \end{cases} \tag{4.14}$$

where *A* represents the amplitude of the incident wave. The value of these three parameters involved in the definition of $h(x)$, namely α and the pair (R, T), can be obtained by a fit of the experimental data in each of the two far-field regions. Although, in this case, α could be determined from the knowledge of the wavenumber *k* through (4.11), it is observed that data adjustment provides more robust results. Indeed, for frequencies near the waveguide cutoff for propagation ($k \lesssim \pi/(2d)$), such a
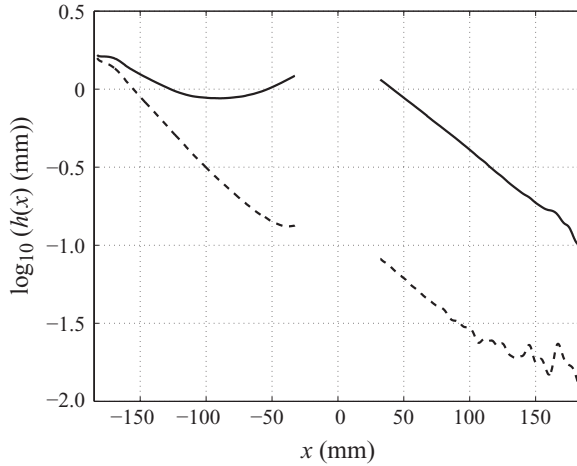
FIGURE 16. Comparison between two typical profiles of $h(x)$ employed for the determination of the reflection and transmission coefficients leading to the resonance curves shown in figure 17.

strategy could effectively lead to considerable error as it would involve the calculation of the square root near a vanishing quantity.

To achieve such a determination, two different strategies have been used. When the whole signal has sufficiently large amplitude (above the threshold for resolution of the measuring method, about 0.2 mm), (α, AT) are fitted from (4.14) in the second region. Similarly, the pair (A, AR) is determined in the first region. This is the case for frequencies near the resonance. However, far from resonance, the amplitude in the second region is very weak, often below the threshold for detection. In these cases, the pair (α, A) is determined near the entrance of the waveguide (reflection is neglected here), afterwards we get rough estimates of (R, T) at the vicinity of the cylinder. These behaviours are illustrated in figure 16: at resonance (plain line), the signal amplitude remains of the order of a millimetre, allowing for a precise adjustment of the data. In contrast, corresponding results for a pulsating frequency 15 % away from the resonance value (dashed curve) show that the amplitude decreases by a factor of 10 before even reaching the cylinder. This leaves most of the signal in region II below the threshold for detection.

Resonance curves obtained for several aspect ratios a/d considered in this study are shown in figures 17(a)–(h). Each panel shows the absolute values of the reflection (plain circles) and transmission (open circles) coefficients as a function of the non-dimensional parameter kd. For $a/d \leqslant 0.8$, a resonance is visible, corresponding to an NS-trapped mode, whereas for $a/d \geqslant 0.85$, a second resonance appears near the cutoff frequency, associated with an NA-trapped mode. Nevertheless, the error on these coefficients becomes important away from the resonance, and no quantitative estimation of the error can be made. Near the resonances, the relative uncertainties in the determination of (R, T) can be evaluated to reach values of up to 30 % in the worst case of the NA-trapped-mode resonances.

4.3.3. *Theoretical study of the resonance*

An interesting feature is the marked asymmetry that is present in the resonance curves around their peak values. This corresponds to a behaviour which cannot be adequately described by means of the classical Breit–Wigner resonant shape. We have verified that this is not an experimental artefact by computing these
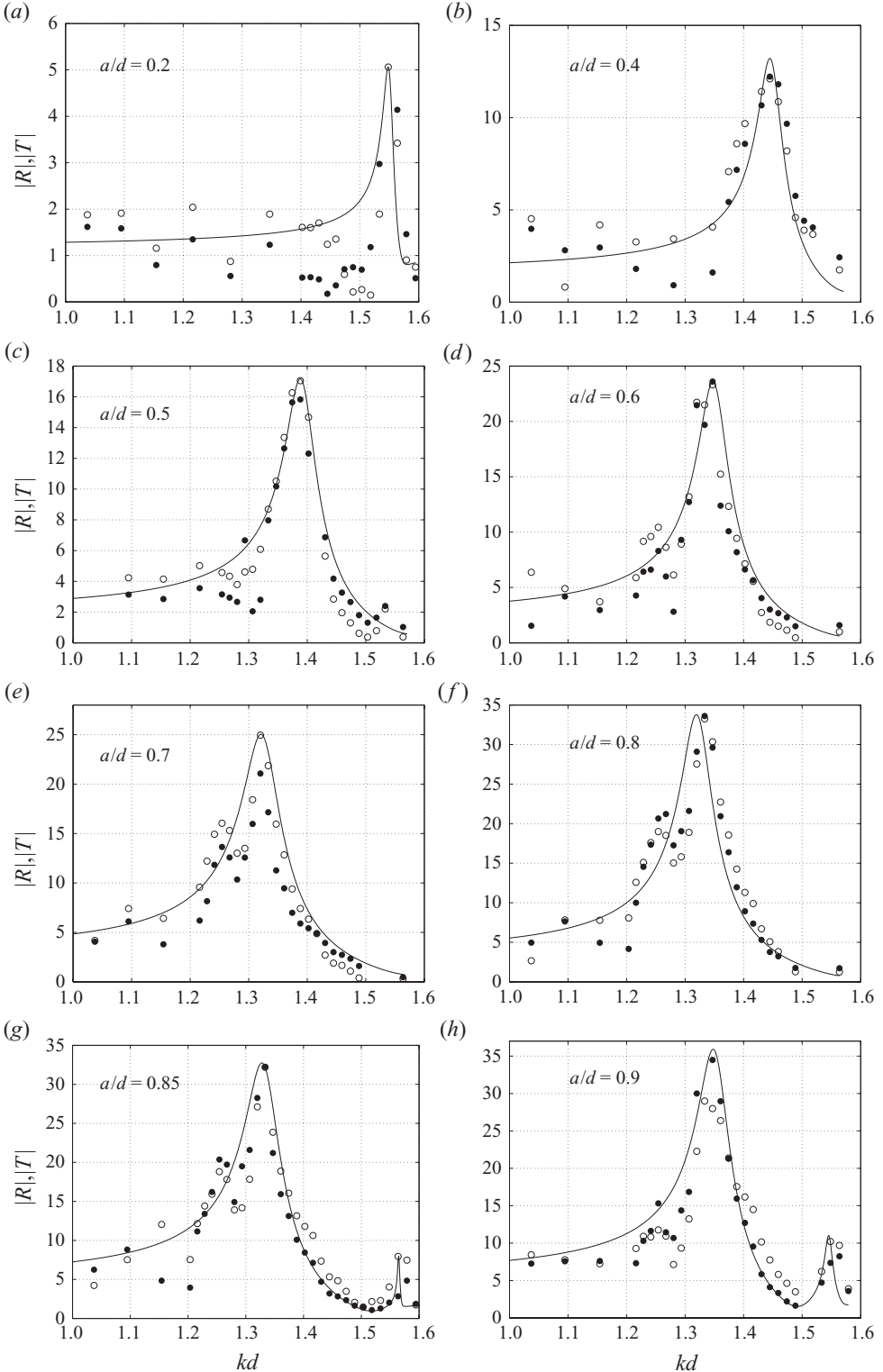
FIGURE 17. Resonance curves for several values of the aspect ratio a/d considered in this study. Full circles: reflection coefficient R; open circles: transmission coefficient T. The continuous line represents the fit of the experimental data (see text for details).

coefficients numerically. For that purpose, we employed the PDEtools toolbox from MATLAB (finite-element method). We solve the Helmholtz equation $(\nabla^2 + k^2)\phi = 0$ with Neumann boundary conditions at the boundaries (walls and obstacle). Then the transmitted and reflected waves are collected, allowing us to recover only the first evanescent mode, as the others (generated in the near field of the cylinder) decrease more rapidly with distance.

The asymmetry of the curves is recovered and follows the expression given by

$$T = \frac{B}{1 - C/(\alpha d)}. \tag{4.15}$$

This relation was proposed by Granot (2002) for bound states in weakly bent waveguides, to describe the resonant behaviour of the scattering taking into account the distortion of the symmetric Breit–Wigner profile due to the proximity of the cutoff frequency. This equation is valid in the neighbourhood of the resonance in the complex k-plane, and describes the resonance profile much more accurately than that of Breit–Wigner. We have numerically checked that (4.15) is a very good approximation with the numerically calculated T in the k-complex plane below the cutoff threshold. Figure 18 shows the dependence of the parameters B, C for both resonances as a function of the aspect ratio a/d. A simple fit for B gives $B = 1 + 1.35 \, (a/d)^3$.

The theoretical curves corresponding to (4.15) are shown as solid lines in figure 17 for each of the aspect ratios explored. For constructing these curves, the attenuation law must be known. In the experiments, a small attenuation is present that is modelled by a small imaginary part of k. This attenuation can be evaluated only roughly because of a low signal-to-noise ratio on the imaginary part of α even at resonance. The experimental measurements of α derived employing (4.11) provide an estimate of $\mathrm{Im}(k)d \sim 0.03$. As shown in figure 17, a good agreement is observed between the experimental data and theoretical prediction given by (4.15), for values of the attenuation coefficient consistent with this estimation for the single-peak resonance curves shown in figures 17(*a–f*). For these curves, the attenuation coefficient $\mathrm{Im}(k)d$ has been chosen within the range $[0.027, 0.03]$ for $a/d > 0.3$, whereas for smallest aspect ratios, $\mathrm{Im}(k)d \sim 0.01$ was observed to provide better results. For the doubly peaked resonance curves shown in figures 17(*g* and *h*), the second resonance that is a visible fact can be reproduced only assuming a significant decrease in the attenuation of about a factor of 10.

4.3.4. *Dependence on the geometry*

In this section, we consider the dependance of the resonant trapped-mode frequency on the obstacle size. Figure 19 shows the resonant frequencies $k_c d$ for each of the aspect ratios a/d studied. In the figure, open circles denote the experimental values corresponding to the maxima of the resonance curves obtained previously. There are two branches: the first (lower curve) correspond to NS-trapped modes and the second to NA-trapped modes (upper curve). The theoretical results are compared to the theoretical prediction by Callan *et al.* (1991) for the first branch, and with the theoretical prediction of Evans & Porter (1999) for the second branch. Evans & Porter (1999) predicted that the resonances of the second branch exist for $a/d \gtrsim 0.81$. This prediction is confirmed here. An excellent agreement is observed with the theoretical predictions available for both branches.

We now turn our attention to the peak values in the resonance curves obtained for the different aspect ratios considered in this study (some of which are shown in figure 17), i.e. the maximum values of both the reflection and transmission coefficients.
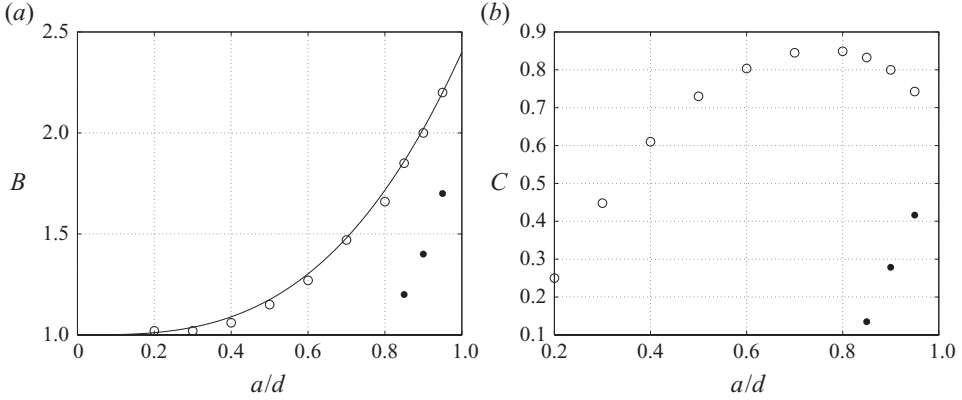
FIGURE 18. Parameters B, C of the transmission coefficient T in (4.15) at resonance as a function of a/d. Open circles correspond to the first resonance (NS-trapped mode), whereas full circles denote the second resonance (NA-trapped mode).
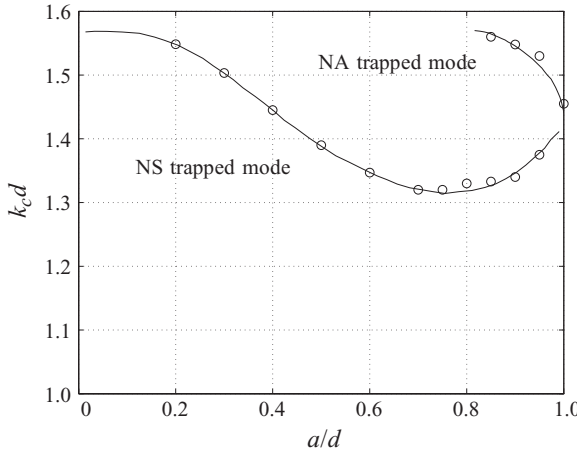

FIGURE 19. Variation of the trapped-mode frequency parameter $k_c d$ with a/d, the ratio of cylinder radius to channel half-width. The continuous line represents the theoretical predictions by Callan *et al.* (1991) (for NS-type trapped modes) and Evans & Porter (1999) (for NA-type trapped modes); circles summarize the experimental results obtained in this study for the two types of trapped modes observed.

For a particular value of the geometrical parameter a/d, these values quantify the maximum amplification rate of the incident wave's antisymmetric part due to the occurrence of the trapped mode.

The dependence of this amplification rate on the aspect ratio is depicted in figure 20 for the NS-type trapped modes. This result shows that the behaviour of the amplification rate (peak values of the reflection and transmission coefficients) can be well described by a linear increase as the ratio of cylinder radius to channel half-width increases.

4.3.5. *From trapped to edge mode*

The case of the totally obstructing cylinder $a/d = 1$ deserves closer inspection. In this case, the trapped mode becomes an edge mode, i.e. a trapped mode in a semi-infinite waveguide, as detailed for elastic plates by Pagneux (2006), or for water
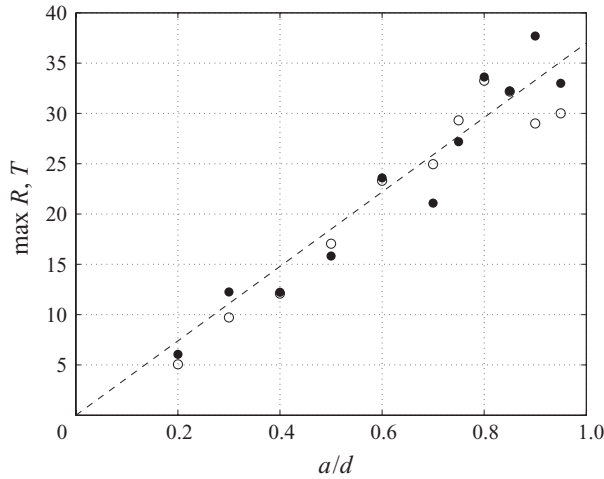
FIGURE 20. Amplification rate of the antisymmetric part of the incident wave (NS-trapped mode at resonance) as a function of the aspect ratio a/d. Peak values of the reflection and transmission coefficients increase in a manner that is essentially linear with the ratio of cylinder radius to channel half-width.
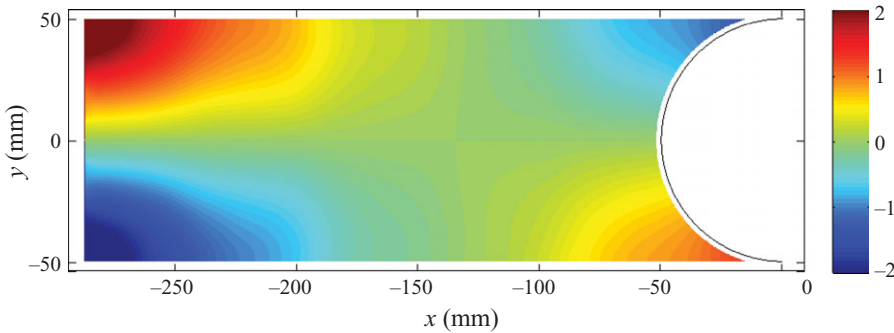

FIGURE 21. Edge mode experimentally observed for $a/d = 1$ and $kd = 1.44$. The position of the obstacle is indicated by the black circle. The scale of the colourbar is in millimetres.

waves in McIver *et al.* (1998), where it corresponds to trapped-mode solutions in a semi-infinite guide with a protrusion at the end.

It is linked to the degeneracy of the symmetric and antisymmetric trapped modes and thus to the intersection between the two branches of resonance in figure 19. Experimentally, the resonance frequency of the edge mode is found at $kd = 1.44$. Figure 21 shows the pattern of the trapped mode, which corresponds to the antisymmetric field associated to the linear part of the experimentally measured FSD.

5. Summary and conclusions

In this study, we have presented experimental evidence of the occurrence of trapped modes around a vertical surface-piercing circular cylinder placed symmetrically

between the walls of a long but finite water waveguide. Using an optical profilometric technique, we were able to measure the space–time evolution of the FSD within the guide.

By decomposing the surface deformation in terms of the harmonics of the driving frequency, we were able to isolate the dominant linear contribution from the higher order harmonics. Further separation of the FSD into symmetric and antisymmetric parts with respect to the centreplane of the channel led us to the recovery of the detailed structure of the trapped mode.

The trapped-mode spatial structure was determined for several aspect ratios a/d, and two types of trapped modes were observed. In particular, only one trapped mode of type NS was observed for each value of a/d explored within the frequency range (always below the waveguide cutoff). A second trapped mode of type NA was observed for $a/d = 0.85$, 0.90 and 0.95, consistent with the theoretical predictions.

The detailed spatial structure of the experimentally observed trapped mode was compared to the predictions of a linear multipole expansion method, showing good overall agreement for various a/d.

For every value of a/d explored, the eigenfrequencies of the trapped modes were determined. To this end, one-dimensional reflection and transmission coefficients within the guide were introduced, allowing for the construction of resonance curves. It is worth noting that such a complete characterization of the scatterer system in terms of reflection and transmission coefficients is rather rare in practice due to the difficulties associated with their experimental determination. In these curves, the presence of a sharp peak evidences the occurrence of a trapped mode. Only for the largest cylinders, these curves show two peaks, the second one corresponding to NA-type trapped modes.

Finally, all the results of this study were summarized in a curve that shows the dependance of the trapped mode (dimensionless) wavenumber $k_c d$ on the aspect ratio a/d. This curve is composed of two branches, corresponding to NS- and NA-type trapped modes. Comparison to theoretical predictions available within the frame of the linear theory shows excellent agreement for both branches. This is indicative of the fact that many effects not considered in the theory (such as viscosity, surface tension, nonlinearities and finite size) are negligible for the description of the trapped modes resonance.

Finally, the case for which the cylinder's diameter coincides with the waveguide width, namely $a/d = 1$, is of particular interest as no theoretical predictions are available. In this case, the trapped mode becomes an edge mode, corresponding to the degeneracy of the symmetric and antisymmetric trapped modes and thus to the intersection of the two branches of resonance.

REFERENCES

CALLAN, M., LINTON, C. M. & EVANS, D. V. 1991 Trapped modes in two-dimensional waveguides. *J. Fluid Mech.* **229**, 51–64.

COBELLI, P. J., MAUREL, A., PAGNEUX, V. & PETITJEANS, P. 2009 Global measurement of water waves by Fourier transform profilometry. *Exp. Fluids* **46**, 1037–1047.

EVANS, D. V., LEVITIN, M. & VASSILIEV, D. 1994 Existence theorems for trapped modes. *J. Fluid Mech.* **261**, 21–31.

Evans, D. V. & Linton, C. M. 1991 Trapped modes in open channels. *J. Fluid Mech.* **225**, 153–175.

Evans, D. V. & McIver, P. 1991 Trapped waves over symmetric thin bodies. *J. Fluid Mech.* **223**, 509–519.

Evans, D. V. & Porter, R. 1997a Near-trapping of water waves by circular arrays of vertical cylinders. *Appl. Ocean Res.* **19**, 83–89.

Evans, D. V. & Porter, R. 1997b Trapped modes about multiple cylinders in a channel. *J. Fluid Mech.* **339**, 331–356.

Evans, D. V. & Porter, R. 1999 Trapping and near-trapping by arrays of cylinders in waves. *J. Engng Math.* **35**, 149–179.

Evans, D. V. & Porter, R. 2002 An example of non-uniqueness in the two-dimensional linear water-wave problem involving a submerged body. *Proc. R. Soc. Lond.* A **454**, 3145–3165.

Granot, E. 2002 Emergence of a confined state in a weakly bent wire. *Phys. Rev.* B **65** (23), 233101.

Harter, R., Abrahams, I. D. & Simon, M. J. 2007 The effect of surface tension on trapped modes in water-wave problems. *Proc. R. Soc.* A **463**, 3131–3149.

Huntley, D. A. & Bowen, A. J. 1973 Field observations of edge waves. *Nature* **243**, 349–365.

Johnson, R. S. 2007 Edge waves: theories past and present. *Phil. Trans. R. Soc.* A **365**, 2359–2376.

Jones, D. S. 1953 The eigenvalues of $\nabla^2 u + \lambda u = 0$ when the boundary conditions are given in semi-infinite domains. *Proc. Camb. Phil. Soc.* **49**, 668–684.

Kuznetsov, N. G. & McIver, P. 1997 On uniqueness and trapped modes in the water-wave problem for a surface-piercing axisymmetric body. *Q. J. Mech. Appl. Math.* **50** (4), 565–580.

LeBlond, P. H. & Mysak, L. A. 1978 *Waves in the Ocean*. Elsevier.

Linton, C. M. & Evans, D. V. 1992 Integral equations for a class of problems concerning obstacles in waveguides. *J. Fluid Mech.* **245**, 349–365.

Linton, C. M. & McIver, M. 2002 The existence of Rayleigh–Bloch surface waves. *J. Fluid Mech.* **470**, 85–90.

Linton, C. M. & McIver, P. 2001 *Handbook of Mathematical Techniques for Wave/Structure Interactions*. CRC Press.

Linton, C. M. & McIver, P. 2007 Embedded trapped modes in water waves and acoustics. *Wave Motion* **45**, 16–29.

Londergan, J. T., Carini, J. & Murdock, D. 1999 *Binding and Scattering in Two-Dimensional Systems: Applications to Quantum Wires, Waveguides and Photonic Crystals*. Springer-Verlag.

Maniar, D. H. D. & Newman, J. N. 1997 Waves diffraction by a long array of cylinders. *J. Fluid Mech.* **339**, 309–330.

Maurel, A., Cobelli, P. J., Pagneux, V. & Petitjeans, P. 2009 Experimental and theoretical inspection of the phase-to-height relation in Fourier transform profilometry. *Appl. Optics* **48**, 380–392.

Maurel, A., Pagneux, V. & Wesfreid, J. E. 1995 Mean flow correction as non linear saturation mechanism in instabilities. *Europhys. Lett.* **32** (3), 217–222.

McIver, M. 1996 An example of non-uniqueness in the two-dimensional linear water wave problem. *J. Fluid Mech.* **315**, 257–266.

McIver, M. 2000 Trapped modes supported by submerged obstacles. *Proc. R. Soc. Lond.* A **456**, 1851–1860.

McIver, M. & Porter, R. 2002 Trapping of waves by a submerged elliptical torus. *J. Fluid Mech.* **456**, 277–293.

McIver, P. 1991 Trapping of surface water waves by fixed bodies in channels. *Q. J. Mech. Appl. Maths* **44** (2), 193–208.

McIver, P. 2002 Wave interaction with arrays of structures. *Appl. Ocean Res.* **24**, 121–126.

McIver, P. & Evans, D. V. 1985 The trapping of surface waves above a submerged, horizontal cylinder. *J. Fluid Mech.* **151**, 243–255.

McIver, P., Linton, C. M. & McIver, M. 1998 Construction of Trapped Modes for Wave Guides and Diffraction Gratings. *Proc. R. Soc. Lond.* A **454**, 2593–2616.

McIver, P. & McIver, M. 1997 Trapped modes in an axisymmetric water wave problem. *Q. J. Mech. Appl. Math.* **50** (2), 165–178.

McIver, P. & McIver, M. 2006 Trapped modes in the water-wave problem for a freely floating structure. *J. Fluid Mech.* **558**, 53–67.

McIver, P. & Newman, J. N. 2003 Trapping structures in the three-dimensional water-wave problem. *J. Fluid Mech.* **484**, 283–302.

Pagneux, V. 2006 Revisiting the edge resonance for lamb waves in a semi-infinite plate. *J. Acoust. Soc. Am.* **120** (2), 649–656.

Postnova, J. & Craster, R. V. 2008 Trapped modes in elastic plates, ocean and quantum waveguides. *Wave Motion* **45** (4), 565–579.

Protas, B. & Wesfreid, J. E. 2002 Drag force in the open-loop control of the cylinder wake in the laminar regime. *Phys. Fluids* **14** (2), 810–826.

Retzler, C. H. 2001 Trapped modes: an experimental investigation. *Appl. Ocean Res.* **23**, 249–250.

Stokes, G. G. 1846 Report on recent researches in hydrodynamics. In *Report to 16th Meeting Brit. Assoc. Adv. Sci., Southampton, Murrey, London*, pp. 1–20.

Takeda, M., Ina, H. & Kobayashi, S. 1982 Fourier-transform method of fringe-pattern analysis for computer-based topography and interferometry. *J. Opt. Soc. Am.* **72**, 156.

Takeda, M. & Mutoh, K. 1983 Fourier transform profilometry for the automatic measurement of 3-D object shapes. *Appl. Opt.* **22**, 3977–3982.

Ursell, F. 1951 Trapping modes in the theory of surface waves. *Proc. Camb. Phil. Soc.* **47**, 1346–358.

Ursell, F. 1952 Edge waves on a sloping beach. *Proc. R. Soc.* A **214**, 79–97.

Ursell, F. 1987 Mathematical aspects of trapping modes in the theory of surface waves. *J. Fluid Mech.* **183**, 421–437.

Zernov, V., Pichugin, A. & Kaplunov, J. 2006 Eigenvalue of semi-infinite elastic strip. *Proc. R. Soc. Lond.* A **462**, 1255–1270.